



## D1.5 – GNSS Solution Report

Deliverable ID	D1.5
Deliverable Title	GNSS Solution Report
Work Package	WP1
Dissemination Level	PUBLIC
Version	1.8
Date	2019-12-13
Status	Text
Lead Editor	LINKS
Main Contributors	LINKS, ENAC

Published by the ASTRail Consortium



## Document History

Version	Date	Author(s)	Description
0.0	2019-01-11	LINKS-NavSAS	Creation of the document.
1.0	2019-01-15	LINKS-NavSAS	First draft of the NavSAS contribution inserted
1.2	2019-01-19	LINKS-NavSAS	Added figures.
1.3	2019-01-31	LINKS-NavSAS	Correction of the legend in Figure 11 and Figure 12.
1.4	2019-02-08	LINKS-NavSAS	Contribution inserted in section 4, conclusions outlined
1.5	2019-02-11	LINKS-NavSAS and LINKS-MLW	Added MLW contribution to subsection 3.2.5 and the introductory paragraph of section 2.3. Revised plots in section 3.2.6 (corrected the travelled distance in the x axis).
1.6	2019-02-24	ENAC	Added sections and revised formatting.
1.7	2019-02-28	LINKS-NavSAS	Formatting revised, typos and references fixed.
1.8	2019-12-13	LINKS-NavSAS	Acronyms table inserted in Section 6.

## Legal Notice

*The information in this document is subject to change without notice.*

*The Members of the ASTRail Consortium make no warranty of any kind with regard to this document, including, but not limited to, the implied warranties of merchantability and fitness for a particular purpose. The Members of the ASTRail Consortium shall not be held liable for errors contained herein or direct, indirect, special, incidental or consequential damages in connection with the furnishing, performance, or use of this material.*

*The Shift2Rail JU cannot be held liable for any damage caused by the Members of the ASTRail Consortium or to third parties as a consequence of implementing this Grant Agreement No 777561, including for gross negligence.*

*The Shift2Rail JU cannot be held liable for any damage caused by any of the beneficiaries or third parties involved in this action, as a consequence of implementing this Grant Agreement No 777561.*

*The information included in this report reflects only the authors' view and the Shift2Rail JU is not responsible for any use that may be made of such information.*

## Table of Contents

Document History .....	2
Legal Notice .....	2
Table of Contents .....	3
1 Introduction .....	4
1.1 Scope .....	4
1.2 Organization of the document .....	4
1.3 Related documents .....	4
2 Architectures .....	5
2.1 Introduction .....	5
2.2 VB Odometry Diagnosis Architecture .....	5
2.3 Accuracy Enhancing Architecture .....	10
3 Test Plans and Models and Results .....	12
3.1 VB Diagnosis Models and Test Definition .....	12
3.2 Accuracy Enhancing Architecture .....	15
4 Algorithms for enhanced robustness against RFI: performance analysis .....	25
4.1 Tracking capability and noise performance analysis .....	25
4.2 Filtering efficiency analysis in a GNSS receiver .....	31
4.3 Final remarks .....	34
5 Conclusions .....	34
6 Acronyms .....	35
List of figures .....	36
List of tables .....	37
References .....	37

## 1 Introduction

This document is the deliverable D1.5 of the ASTRail project; it includes the outcomes of Task 1.7 “GNSS Algorithm Performance Assessment and Verification” carried out by LINKS and ENAC. In particular, ENAC worked on the algorithms for the limitation of Global Navigation Satellite Systems (GNSS) failures in a GNSS-centric architecture, whereas LINKS carried out the activity about the enhancement of both the positioning solution availability and the robustness against Radio-Frequency Interference (RFI).

### 1.1 Scope

As already mentioned in [RD.2], the introduction of the GNSS technology in safety railway applications is the new challenge. A safe train positioning is, indeed, one of the technical demonstrator of the Innovation Programme 2 (IP2) – Advanced Traffic Management and Control Systems – of the EU-H2020 Shift2Rail (S2R) project [1], aiming to develop a fail-safe, multi-sensor GNSS-based train positioning system as an add-on to the current European Rail Traffic Management System/European Train Control System (ERTMS/ETCS).

In [RD.2], the main impairments affecting the GNSS signal in a railway scenario, i.e. multipath and RFI, have been classified and discussed. In [RD.3] a GNSS-centric architecture is presented and algorithms for the limitation of GNSS failures, and the enhancement of both the positioning solution availability and the robustness against RFI have been proposed.

In this deliverable the performance evaluation of the algorithms selected in [RD.3] is presented.

### 1.2 Organization of the document

After the Introduction, this document can be divided in three main parts

- Section 2 describes the architectures
- Section 3 presents the test plans, simulation and processing models for the two architectures given in section 2 including a selection of a subset of complementary technologies, among all the ones proposed in [RD.3], and their integration with the GNSS.
- Section 4 reports the performance assessment of the RFI detection and mitigation algorithm selected in [RD.3].

Finally, Section 5 draws some conclusions.

### 1.3 Related documents

ID	Title	Reference	Version	Date
[RD.1]	D1.1 – Aeronautical Assumptions and Requirements	ASTRAIL_D1.1	V1.5	01/02/2019
[RD.2]	D1.2 – Local GNSS Effects	ASTRAIL_D1.2	V1.0	28/02/2018
[RD.3]	D3.2 - Automatic Train Operations: implementation, operation characteristics and technologies for the Railway field	ASTRAIL_D3.2	V1.0	28/02/2018
[RD.4]	D3.1 –State of the Art of Automated Driving technologies	ASTRAIL_D3.1	V1.1	01/06/2018

## 2 Architectures

In this section, the architectures which have been considered during the task T1.7 are outlined. The ASTRail project began following the Virtual Balise architecture [RD.1] and has also addressed the feasibility and benefits of additional sensors [RD.3]. In the proceeding section 3 tests and simulation models are presented for these two architectures.

### 2.1 Introduction

Considered in this work are two uses of odometry like sensors. Odometry sensors include wheel speed sensors, doppler radar and might also feasible include inertial sensors, video and others [RD.3]. In this work, given the scope and constraints of the project, odometry is limited to wheel speed sensors which are available in all train installations and doppler radar which might potentially be available. The addition of inertial sensors in the single train axis in order to augment the odometry could be considered but is omitted here due to modelling complexity.

The two uses of odometry here are with different goals. In the first, described in section 2.2 odometry is used as a means to verify the GNSS between physical balises which are intended to be spaced at much greater distance, in particular on long sections. In the second, described in section 2.3, odometry is integrated with the GNSS with the aim of providing a more accurate solution rather than monitoring the GNSS.

### 2.2 VB Odometry Diagnosis Architecture

The use of GNSS in the railway sector has been postulated on the notion of a Virtual Balise (VB). Existing railway positioning systems are based on various trackside infrastructures including Physical Balises (PBs) installed in groups between the tracks and odometry installed on-board. However, due to the high cost of installing and maintaining the PB, a GNSS-based VB positioning performed within on-board system has been proposed to reduce the role of PBs. Importantly however, the use of VBs will enable backward compatibility with existing architectures supporting PBs to accelerate and simplify the adoption of VBs.

The VB-based positioning system works by setting a VB point on the railway track and determining the passage of the VB point using the position solution from the GNSS receiver, replacing the existing PB. The actual PB delivers a message depending upon the direction of travel at the time of passing. The VB therefore must support similar capabilities.

As mentioned above, high safety requirements are required in the railway sector. Augmentation systems such as SBAS or GBAS, which are widely used in the aviation sector, are able to satisfy the integrity requirements of the aviation standards down to the  $10^{-7}$  per hour level. However, it is difficult to satisfy the high integrity requirements of the railway sector because firstly the signals employed by railway users located on the ground are affected by the ground environment such as terrain, buildings and tunnels and secondly because the stringency of the requirements extends below the  $10^{-9}$  level. Furthermore, at such a safety integrity level, rail requirements must be met through the provision of multiple functions. It is for this reason that previous research has proposed the use of odometry to help verify the absence of GNSS faults [1]. There are several researches focused on improving position accuracy or integrity by introducing additional sensors or information such as a sky-view camera [3], inertial measurement unit [4] and track map [5]. Usage of new sensors which are not embedded in the original system requires additional cost and complexity.

This work proposes a method to detect faults in the GNSS solution due to satellite failure or local effects in advance of improving positioning accuracy. Firstly, requirements are derived accounting for the specificities of GNSS, namely that the possibility of consecutive VB faults cannot be discounted, which has not been fully considered in some previous studies [6]. Such an assumption leads to requirements for the detection, or

diagnosis of a GNSS fault through odometry, in terms of the duration of hazardous and not just the probability of occurrence.

Secondly a proposed detection using both odometry and track geometry of the onboard system is made. Especially, track geometry is useful for monitoring the deviations both laterally (across track) and vertically and detecting for the presence of ranging faults that may also impact the along track solution. Exponentially weighted moving averages (EWMA) of the difference in relative position change between GNSS, odometry and track geometry are derived. Currently a bank of four such metrics are used with varying scale averaging parameter. The combination of metrics enables the monitoring solution to detect both quickly varying faults, such as jumps or sharp ramps as well as slowly varying faults which ultimately, are the more difficult to detect.

The positioning function plays important role in the automation of train. The Localization Unit (LU) determines the position of the train and transmits it to the trackside infrastructure. Using this information, the control system decides whether a movement authority can be given or not to the train. Existing positioning function of European Train Control System (ETCS) computes the position of a train based on the use of trackside infrastructure including *Eurobalises* and odometry. The Eurobalise is a PB which is installed on railway track and transmits a signal when a train passes over in one intended direction. The transmitted signal contains identification and position information of the PB. PBs are installed consecutively along railway track with specific interval. Average distance of 2 km between PBs is usually adopted in Europe for high speed train up to 300 km/h. The odometry function accumulates traveled distance from recently passed PB and provides position while the train is located between PBs. The architecture of PB based positioning function is represented in green blocks in Figure 1. Rail network operators, train manufacturers and rail industry stakeholders are trying to find a way to utilize GNSS to reduce the cost of maintaining current positioning system without alternating its architecture. A VB is proposed to provide positioning function with GNSS. It is compatible with the architecture of the current PB based LU so that the current system can migrate to a partially VB based system without refitting of all subsystems. A VB is a certain point set on the railway instead of the installation of a PB. The LU determines the passage of VB point based on combined position solution from GNSS and odometry. Utilization of correction from augmentation systems is also considered. The architecture of VB is represented in red blocks in Figure 1. GNSS with SBAS or GBAS has successfully provided integrity which meets its standard for aviation. However, providing integrity of GNSS to the railway is challenging because its higher required level of integrity and the effect of ground environment. In the section, hazards of VB based positioning system are classified.

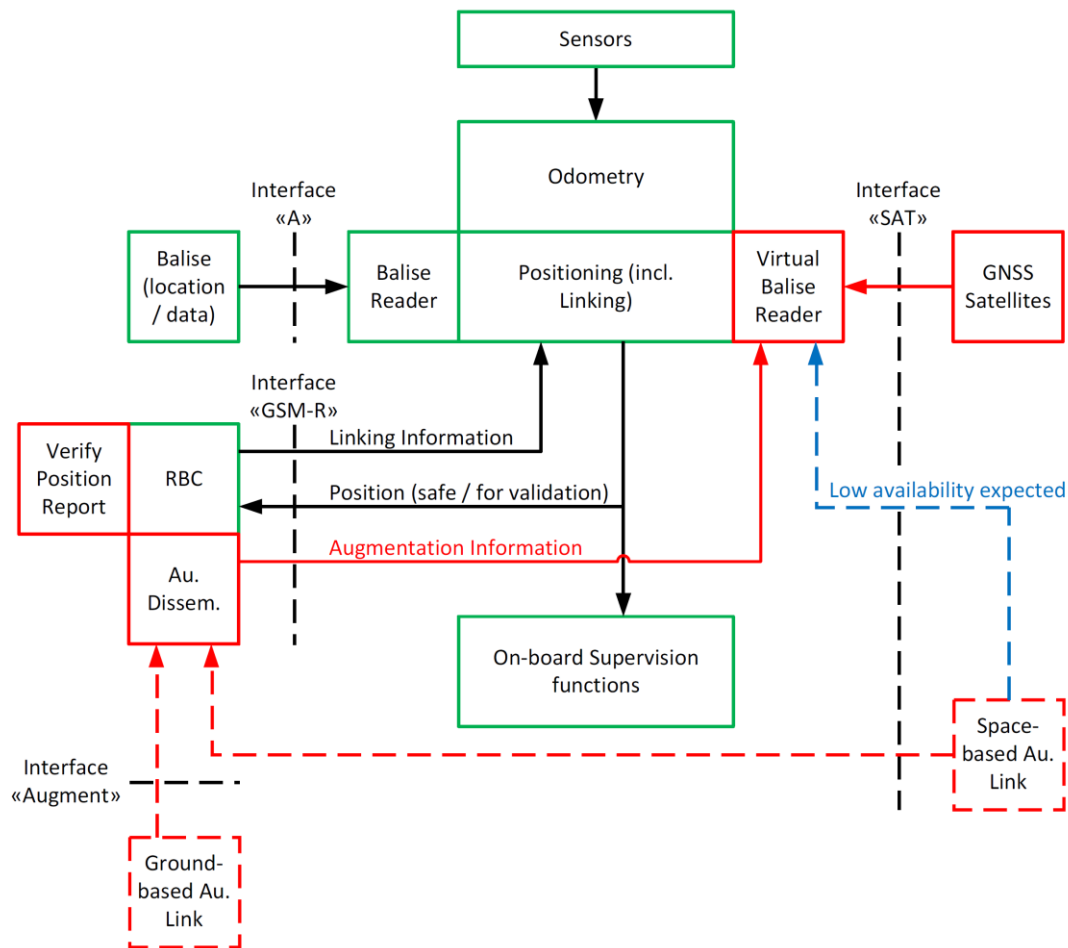


Figure 1 Architecture of localization unit of train [7]

### 2.2.1 Hazards Considered

In the current PB based positioning architecture, three hazards were identified and are listed in [6]. These hazards are *corruption*, *deletion* and *insertion*. The corruption is when transmitted data from a PB contains an erroneous telegram, the deletion is when a PB over which train passes is not detected, and the insertion is when a train detects a PB that it should not (through cross-talk with a PB on a parallel track). The corruption does not need to be considered in VB based system since the transmission from VB will not actually occur and the telegram data will be stored in the LU on the train. Occurrence of a corruption or a deletion was monitored by comparing the order of IDs of detected balises with the expected order of those. Previous work [8] has specified the hazards of VB in a similar manner. However, due to the nature of GNSS faults, the following classification is used here.

**VB Jump (VB-HAZARD 1)** occurs when the position solution jumps from one epoch to the next thereby either crossing multiple virtual balises (VB-HAZARD 1A) or crossing in an excessive manner a single virtual balise (VB-HAZARD 1B).

**VB Shift** occurs when the position error drifts with time thus leading to virtual balise detection which is earlier or later than is correct (VB-HAZARD 2). In the extreme case, with a very high drift, this hazard is equivalent to (VB-HAZARD 1B).

VB Jump is, by definition, the least critical and least challenging. In the case of VB-HAZARD 1A, by checking the order of detected balises enables diagnosis of a GNSS fault and the system passes to a fail-safe state (linking like mitigation). The second sub-case is subtler and requires an odometry based cross-check to diagnose its occurrence. Finally, for the VB shift case, the ability to diagnose such a fault will depend upon the degree of drift between the GNSS and odometry solutions, and it is investigated in this work.

### 2.2.2 Diagnostic monitors

The basic notion of the diagnosis is that comparing the differential position from GNSS with that of odometry to detect fault of GNSS including a drift of position solution induced by a satellite failure or multipath. A raw monitor in the along-track direction at epoch  $k$  is introduced as follows:

$$q^{\Delta x}(k) = \Delta x^{\text{gnss}}(k) - \Delta x^{\text{odo}}(k) \quad (1)$$

$$\Delta x^{\text{gnss}}(k) = x^{\text{gnss}}(k) - x^{\text{gnss}}(k-1) \quad (2)$$

$$\Delta x^{\text{odo}}(k) = x^{\text{odo}}(k) - x^{\text{odo}}(k-1) \quad (3)$$

where  $q^{\Delta x}$  is the raw monitor in the along-track direction,  $x^{\text{gnss}}$  and  $x^{\text{odo}}$  represent positions provided by GNSS and odometer in the along-track direction, respectively.

Assuming that the error components of GNSS and odometer position are zero-mean Gaussian, the statistic of the raw monitor is given by

$$q^{\Delta x}(k) \sim N(0, \sigma_{\Delta x}^2) \quad (4)$$

and variance of the raw monitor represented as

$$\sigma_{\Delta x}^2 = \sigma_{\Delta x, \text{gnss}}^2 + \sigma_{\Delta x, \text{odo}}^2 \quad (5)$$

where

$$\Delta x^{\text{gnss}}(k) \sim N(0, \sigma_{\Delta x, \text{gnss}}^2) \quad (6)$$

$$\Delta x^{\text{odo}}(k) \sim N(0, \sigma_{\Delta x, \text{odo}}^2) \quad (7)$$

For an SBAS-augmented single frequency code user,  $\sigma_{\Delta x, \text{gnss}}$ , the standard deviation of GNSS part is a meter-level and dominant. This raw monitor may be useful for detecting faults over a rate of several meter per second or jumps of several meters. However, it is not effective to detect faults of submeter per second level. Averaging techniques can be applied to the monitor to reduce its standard deviation and to improve detectability for slower faults. Exponential Weighted Moving Average (EWMA) is a sequential averaging technique and its level of averaging effect can be adjusted by setting its weighting parameter  $\alpha$ . The EWMA applied monitor is given by

$$\bar{q}_{\alpha}^{\Delta x}(k) = \alpha \cdot q^{\Delta x}(k) + (1-\alpha) \cdot \bar{q}_{\alpha}^{\Delta x}(k-1) \quad (8)$$

The sequential form of EWMA gives great advantage of saving memory space when a long period of averaging



window is required. The averaging effect of EWMA slows the response of monitor to the fault. Therefore, the following bank of monitors, which constitutes with the raw monitor and EWMA monitors with different  $\alpha$  values, is used.

$$\begin{bmatrix} q^{\Delta x} \\ \bar{q}_{0.1}^{\Delta x} \\ \bar{q}_{0.01}^{\Delta x} \\ \bar{q}_{0.001}^{\Delta x} \end{bmatrix} \quad (9)$$

As odometry provides information of displacement in only the along-track direction, the sensitivity of fault detection can vary with the heading of train. To handle this issue, this work proposes the usage of track geometry information. The position of the train is constrained to be located on the rail track. Therefore, the track geometry or map information can be used to derive a monitor in the cross-track and vertical direction. A ranging error in one specific direction affects the position error in the other directions as well as its direction, so that simultaneous monitoring of all three-dimension can improve the detectability. Raw monitors in the cross-track and vertical direction can be driven as follows by substituting the position information of odometry with that of the track geometry. The raw monitors in the cross-track and vertical direction are given as follows:

$$q^{\Delta y}(k) = \Delta y^{\text{gnss}}(k) - \Delta y^{\text{map}}(k) \quad (10)$$

$$q^{\Delta z}(k) = \Delta z^{\text{gnss}}(k) - \Delta z^{\text{map}}(k) \quad (11)$$

$$\Delta y^{\text{gnss}}(k) = y^{\text{gnss}}(k) - y^{\text{gnss}}(k-1) \quad (12)$$

$$\Delta z^{\text{gnss}}(k) = z^{\text{gnss}}(k) - z^{\text{gnss}}(k-1) \quad (13)$$

$$\Delta y^{\text{map}}(k) = y^{\text{map}}(k) - y^{\text{map}}(k-1) \quad (14)$$

$$\Delta z^{\text{map}}(k) = z^{\text{map}}(k) - z^{\text{map}}(k-1) \quad (15)$$

where  $q^{\Delta y}$  and  $q^{\Delta z}$  are the raw monitors in the cross-track and vertical direction,  $y^{\text{gnss}}$  and  $z^{\text{gnss}}$  represent positions provided by GNSS in the cross-track and vertical direction,  $y^{\text{map}}$  and  $z^{\text{map}}$  represent the cross-track and vertical components of projected GNSS position on railroad curve from the track geometry, respectively. The banks of monitors in the cross-track and vertical direction are also given by

$$\begin{bmatrix} q^{\Delta y} \\ \bar{q}_{0.1}^{\Delta y} \\ \bar{q}_{0.01}^{\Delta y} \\ \bar{q}_{0.001}^{\Delta y} \end{bmatrix}, \begin{bmatrix} q^{\Delta z} \\ \bar{q}_{0.1}^{\Delta z} \\ \bar{q}_{0.01}^{\Delta z} \\ \bar{q}_{0.001}^{\Delta z} \end{bmatrix} \quad (16)$$

With the banks of monitors in place, the thresholds for each monitor must be set as follows:

$$T = k_T \cdot \sigma \quad (17)$$

where  $\sigma$  represents the standard deviation of a monitor,  $T$  is the threshold corresponding to the monitor. The value for  $k_T$  is taken corresponding to 10<sup>-7</sup> of false alarm probability for each monitor. When at least one monitor value exceeds the corresponding threshold, a fault detection is made. The process of fault detection is represented in Figure 2. Note that the thresholds for each direction vary with the heading and satellite

geometry. This variation of threshold is modelled with standard deviation of the along-track GNSS position by a linear regression method.

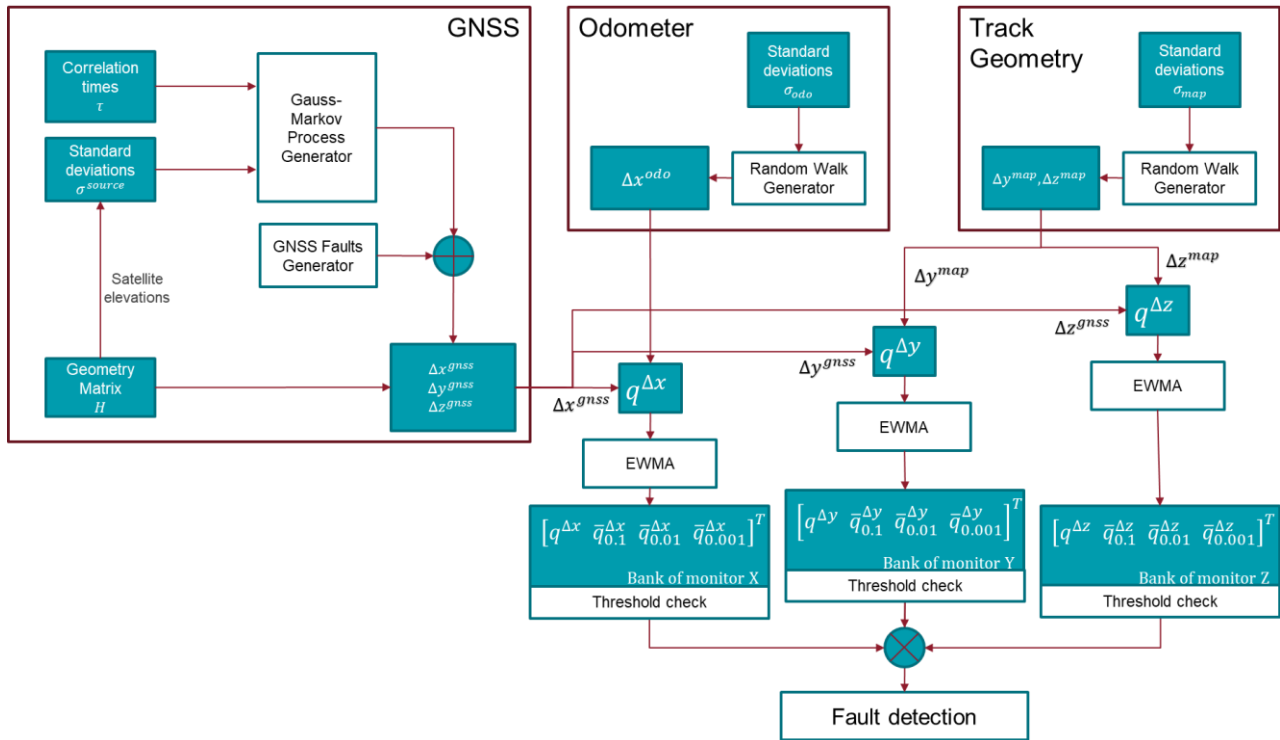


Figure 2 Process of fault detection

### 2.3 Accuracy Enhancing Architecture

To increase the availability and the precision of the GNSS positioning in the presence of a GNSS impaired environment as described in [RD.2], the loosely coupled integration has been implemented. To aid the GNSS receiver, two complementary positioning systems have been chosen taking into account the state-of-the-art analysis presented in [RD.3], both systems are based on dead reckoning technology:

- Doppler Radar;
- Wheel odometer.

Among the several complementary positioning systems that have been introduced in [RD.3], these systems have been selected as exemplary solutions, but any other positioning systems of the previously introduced ones can be considered for the integration into the GNSS centric architecture. This selection has been performed for the availability of information related to performance. The wheel odometer has been selected since it is already largely exploited in the railway domain and model errors of odometer can be found. Doppler Radar is a recently introduced sensor, however, some literature of products' datasheets is available providing information about the achievable performance and error characterization.

The resulting integration algorithm can be represented as in Figure 3.

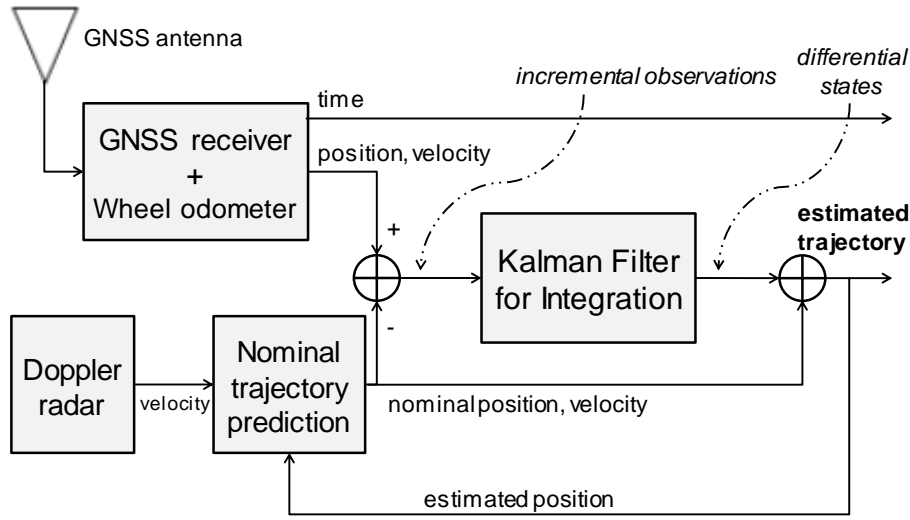


**Figure 3 - Block scheme for the employed loose integration**

Both Doppler radar and wheel odometer provide velocity estimations. Namely, the velocity from the Doppler radar is used for the prediction of the nominal trajectory as in (18).

$$\begin{aligned}\tilde{p}^e[n] &= p^e[n-1] + T_r v^e[n-1] \\ \tilde{v}^e[n] &= v_r^e[n]\end{aligned}\quad (18)$$

Used symbols are coherent with those reported in [RD.3], with the addition of

- $\tilde{x}^e[n] = [\tilde{p}^{eT}[n], \tilde{v}^{eT}[n]]^T$  is the nominal trajectory in the Earth frame, where  $\tilde{p}$  and  $\tilde{v}$  indicate nominal position and nominal velocity respectively;
- $v_r^e$  is the velocity in the Earth frame out of Doppler radar;
- $p^e$  and  $v^e$  are the position and velocity estimated by the Kalman filter;
- $T_r$  is the time between two consecutive outputs from the Doppler radar. It must be noticed that the rate of the Doppler radar can be different from the rates of the GNSS positioning and the wheel odometer: e.g. in our tests  $T_r = 0.1s$  and  $T_c = 1s$  for GNSS and the odometer, but other time interval are possible.

On the contrary, the velocity from the wheel odometer is used as an additional measurement during the KF update phase. The resulting innovation equation is reported by (19) where a simplified expression has been obtained by putting  $\Delta x^-[n] = \mathbf{0}_{6,1}$ , i.e. the predicted differential states have always zero values.

$$\begin{aligned}\alpha[n] &= (z[n] - \tilde{z}[n]) \\ z[n] &= [p_g^{eT}[n], v_g^{eT}[n], v_o^{eT}[n]]^T \\ \tilde{z}[n] &= [\tilde{p}^{eT}[n], \tilde{v}^{eT}[n], \tilde{v}^{eT}[n]]^T\end{aligned}\quad (19)$$

In (19),  $p_g^e$  and  $v_g^e$  are the position and the velocity found by the GNSS receiver, whereas  $v_o^e$  is the velocity out of the wheel odometer. It must be noticed that the measurement arrays are made of 9 elements. Then, the discrete time observation matrix  $H$  can be defined as in (20).

$$H[n] = \begin{bmatrix} I_{3,3} & \mathbf{0}_{3,3} \\ \mathbf{0}_{3,3} & I_{3,3} \\ \mathbf{0}_{3,3} & I_{3,3} \end{bmatrix}\quad (20)$$

Finally, the loose integration algorithm starts working when the first PVT estimation from the GNSS receiver is available, because the complementary systems are not able to provide a positioning solution without an external initialization. This loose integration algorithm has been implemented in Matlab and tested as described in section 3.2.

### 3 Test Plans and Models and Results

In this section the test plans based on simulation and the employed models are presented for the two architectures given in section 2.

#### 3.1 VB Diagnosis Models and Test Definition

##### 3.1.1 Error Models

Modeling of GNSS errors follows previous works [9] and standard assumptions [10]. A Gauss Markov 1<sup>st</sup> order model is assumed for each error source including ionospheric error, tropospheric error, satellite orbit and clock error and the user error consisting of nominal multipath and noise [11]. The ionospheric error and the satellite orbit and clock errors are assumed to be remaining errors after application of SBAS correction. Details of GNSS error model are represented in Table 1.

**Table 1 GNSS Error model parameters**

Error Source	$R(0)$	$\tau$	$\frac{R(\Delta=10s)}{R(0)}$	$\frac{R(\Delta=1s)}{R(0)}$
Units	[m <sup>2</sup> ]	[s]		
Ionosphere	vary /w El [9]	360s	0.9726	0.9972
Troposphere	vary /w El [9]	1800s	0.9945	0.9994
Orbit/Clock	0.3	3600s	0.9987	0.9997
User	1.5	100s	0.9048	0.9900

Two kinds of odometer, tachometer and radar are commonly equipped in train. The tachometer suffers from slipping and sliding when the train is accelerating and braking [2]. The radar shows consistent performance regardless of the movement of train. However, it can be erroneous when the facing ground surface is wet or covered with snow. Considering the described measurement uncertainty in [12] and assumed 1 Hz of measurement usage which is lower than raw output rate of sensor (>10 Hz), it is assumed that the combined odometry of tachometer and radar can give measurement with 0.05 m/s of noise.

Embedded track geometry data is assumed to give the cross-track and vertical coordinate of the train position with 1 m noise considering surveying error, track deformation error, and interpolation error along the surveyed points.

##### 3.1.2 Test Simulation Setup

Single constellation of GPS and dual-constellation of GPS and Galileo were tested in simulation to investigate the advantage of multi-constellation for fault detection. Range error was inserted into GPS satellite #8 for both settings of constellation. The inserted range error was ramp type, and the drift rate from 0.01 m/s to 5 m/s is tested. This range error accounts for a fault of satellite or a multipath error due to objects on the ground. Positioning failure is defined as the excess of 20 m of position error in the along-track direction.

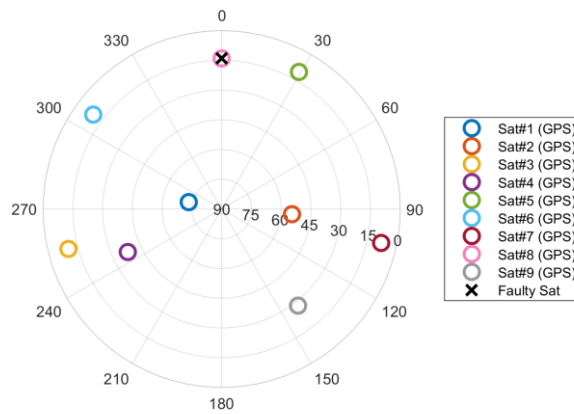


**Figure 4 Skyplot of GPS constellation**

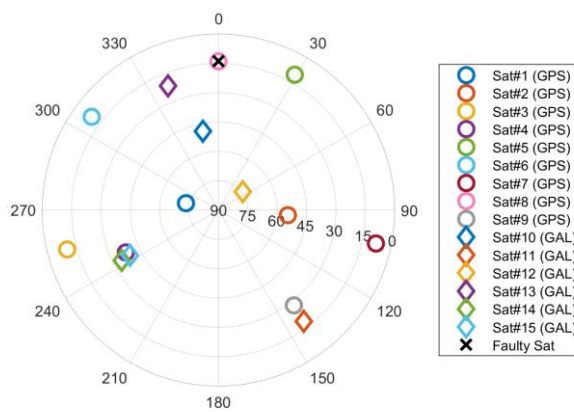


**Figure 5 Skyplot of dual-constellation of GPS and Galileo**

Monte Carlo simulations with  $10^4$  repetitions were performed. Total time span of each simulation run was 15000 secs, and the range error was inserted from 5000 sec. The geometry of satellites and heading of the train were assumed to be fixed during simulation to consider a worst-case where the range error of slow drift rate can generate sufficiently large position error. Various heading of the train from 0 to 75 degrees with steps of 15 degrees are tested to confirm the effect of range error direction.

The results of the probability of missed detection ( $P_{md}$ ) according to the time of detection since positioning failure ( $T_{dsf}$ ) are shown in Figure 6. In the results, the heading angle is zero (the train heads toward the faulty satellite), and only the odometer is used for the diagnosis. The  $T_{dsf}$  means elapsed time from the moment of position failure, when the position error in the along-track direction exceeds 20 m, and a negative value of it means that the fault is detected in advance of the occurrence of position failure. The results of  $P_{md}$  for ramp failure of 0.03 m/s and 0.10 m/s show that the  $P_{md}$  reaches zero when the  $T_{dsf}$  has negative value. This means that the fault in range measurement is detected before the occurrence of position failure for all runs of simulation. The  $P_{md}$  of dual-constellation decreases faster than that of GPS constellation so that the dual-constellation can detect the fault more quickly. However, in case of ramp failure of 0.01 m/s,  $P_{md}$  cannot reach zero for both of constellation cases even after  $T_{dsf}$  reaches positive value. This indicate that not all fault can be detected even after the occurrence of position failure.

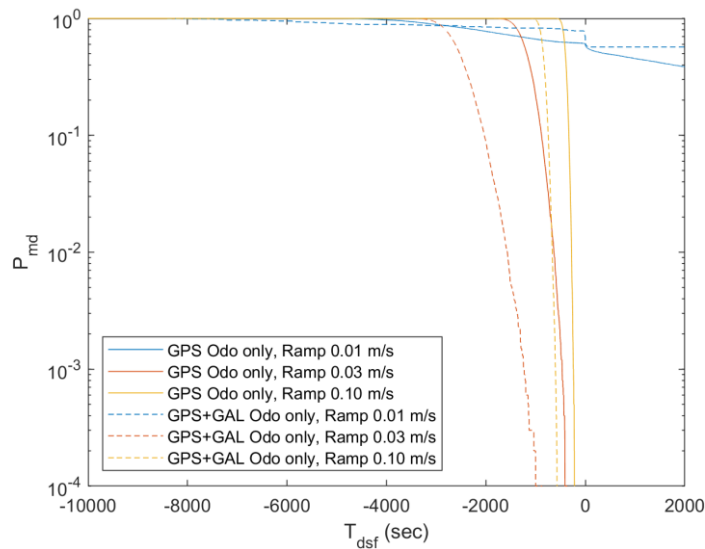


**Figure 6 Results of  $P_{md}$  according to the time of detection since position failure**

The results of expected time of detection ( $T_d$ ) according to variation of heading of the train are represented in Figure 7. The  $T_d$  is the time taken for the detection since the occurrence of fault in range measurement. The results using only odometry show an increase of  $T_d$  when the direction of faulty satellite is deviated from the heading of train since the odometry can provide only displacement information along advancing direction of the train. On the other hand, the track geometry can provide information for across track and vertical directions so that stable detection is possible when the odometry and the track geometry are used together.

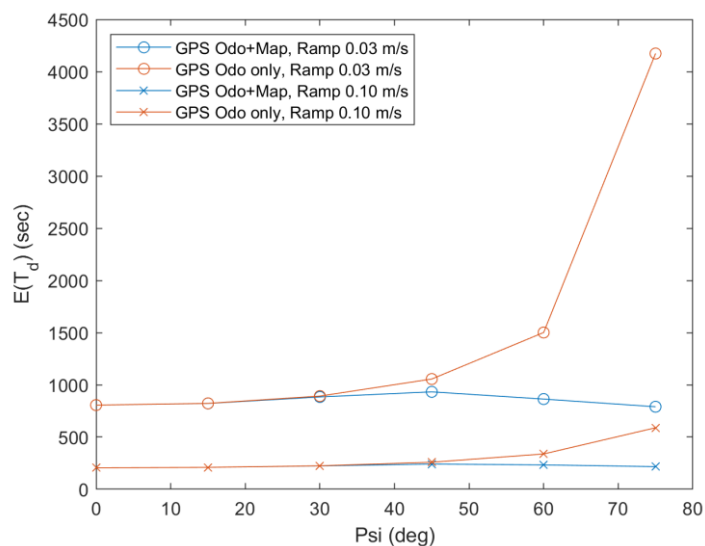


**Figure 7 Expected time of detection according to the heading of train**

The results of expected  $T_{dsf}$  according to various heading of train and drift rate of failure are shown in Figure 8. The expected  $T_{dsf}$  of dual-constellation leads that of GPS constellation case. The larger number of satellites in dual-constellation reduces the influence of fault on position solution, and the occurrence of position failure is postponed. As a result, greater margin of time between the detection of fault and position failure can be achieved.

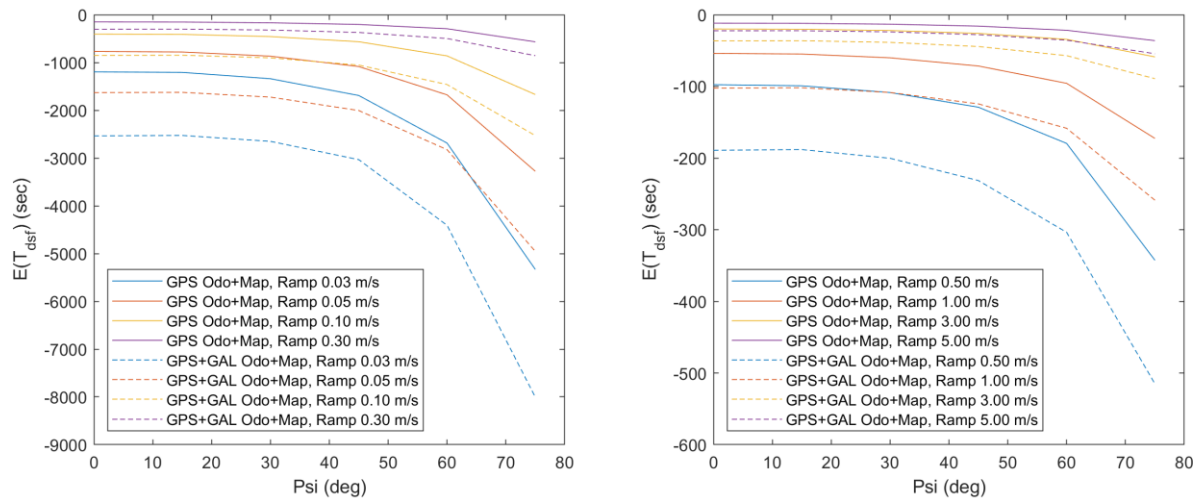


**Figure 8 Time of detection since position failure according to heading of train**

### 3.2 Accuracy Enhancing Architecture

The performed tests are described by Figure 9, each step will be detailed by the following subsections.

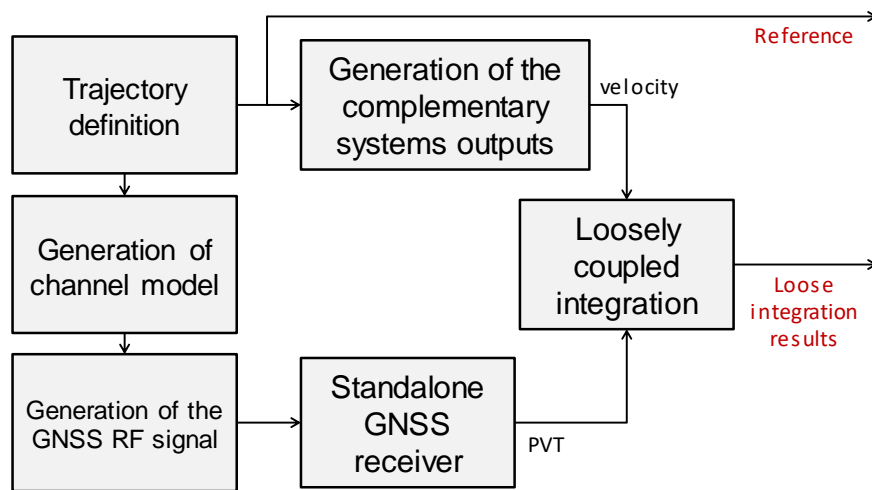


**Figure 9 – How the tests are performed on the loose integration algorithm**

#### 3.2.1 Trajectory definition

The position and the velocity of the train during the simulation is defined for each time instant. The use of a statistical channel model for the simulation of the local channel effects [RD.2] enables the use of an artificial trajectory without decreasing the validity of the final results: the chosen artificial trajectory is a square with rounded corners as depicted by Figure 10. The same kind of trajectory has been used for three tests, one for each scenario described in [RD.2], changing the trajectory parameters as reported in Table 2. This trajectory is also used as the reference to obtain the positioning error of the system.

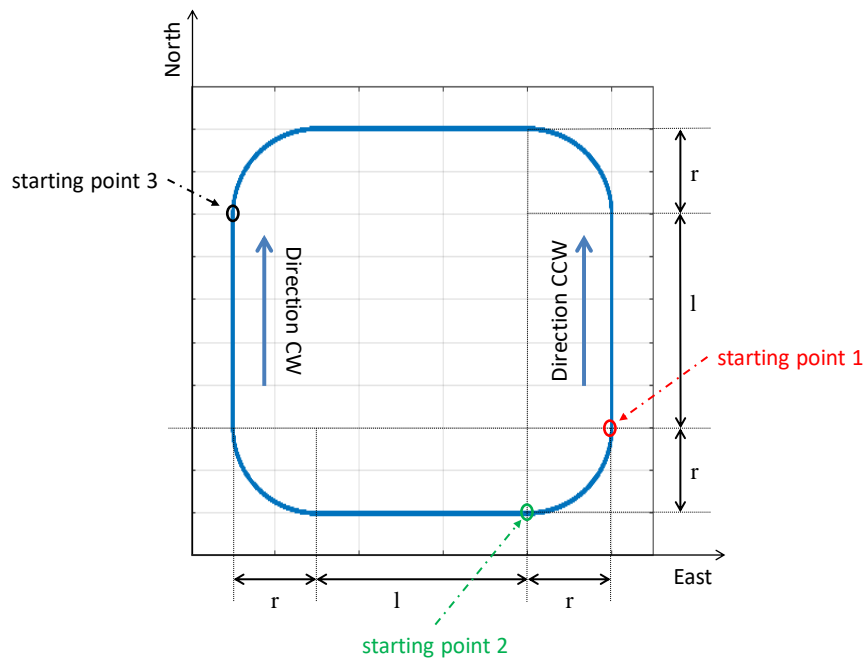


**Figure 10 – Sample artificial trajectory used for the tests**

Simulated scenario	Side length (l)	Turn radius (r)	Maximum velocity	Direction	Starting point	Simulation length	Simulation time
Urban	5 km	2 km	50 km/h	Counter-clockwise (CCW)	Starting point 1	16.0 km	1126 s
Suburban	5 km	2 km	90 km/h	Clockwise (CW)	Starting point 2	14.1 km	563 s
Open sky	5 km	2 km	130 km/h	Counter-clockwise (CCW)	Starting point 3	15.0 km	412 s

**Table 2 – Parameters of the trajectories used during the tests**

### 3.2.2 Generation of channel model

Starting from the trajectories defined in subsection 3.2.1, three channel models have been generated as described in [RD.2], one channel model for each supported scenario, i.e. urban, suburban and open-sky. These statistical channel models simulate the presence of multiple reflections, LOS diffractions and LOS blockages. During these tests, the presence of tunnels with a random length has been simulated by introducing complete outages of the GNSS signals.

### 3.2.3 Generation of the GNSS RF signal

An IFEN NavX-NCS RF signal generator has been used to generate the GNSS signals affected by the local channel effects. The signal generator is configured by using the files obtained as described in [RD.2].

### 3.2.4 Standalone GNSS receiver

The GNSS RF signal is fed to a Septentrio AsteRx4 receiver to get the PVT estimation from the GNSS signal affected by the local channel effects. It must be noticed that, even if the adopted receiver is capable of advanced positioning methods based on the differential corrections (RTK), during these simulations the positioning algorithm performed is a standalone GNSS one, without any external aid.



### 3.2.5 Generation of the complementary systems outputs

The following of this Section provides information about how the velocity outputs of the two selected complementary technologies have been generated.

#### 3.2.5.1 *Wheel odometer*

The wheel odometer velocity has been generated taken into account the ground-truth velocity of the trajectory and varying it to consider the error introduced by the wheel odometer's measurements.

The errors of the velocity measurements have been modelled with a white noise as in this reference paper [14].

The analysis of real data from wheel odometers can lead to achieve a more realistic characterization of the errors introduced by wheel odometers. This is however out of scope of the current activity that aims to assess the impact in the positioning when integrating dead reckoning technologies in a GNSS centric architecture.

#### 3.2.5.2 *Doppler Radar*

The Doppler Radar velocity has been generated in a similar way to the wheel odometer velocity. The ground-truth velocity has been modified to take into account the error introduced by the Doppler Radar.

No error models about Doppler Radar seems to be available in the literature to the best of our knowledge. An error model has been thus defined considering the information retrievable from public available datasheets [15].

The defined error model assumes that the error introduced by the Doppler Radar can be modelled with an additive white noise. The standard deviation has been estimated based on the maximum error that a Doppler Radar can introduce into the velocity measurements. This corresponds to assume that the measurements' errors of a Doppler Radar follows a truncated Gaussian distribution with zero mean and standard deviation computed as previously explained. This assumption is a first approximation, but it is sufficient for the scope of this work. This error model, as for the odometer case, is not meant to be the target of this work, but it was defined for being able to verify the impact of adding dead reckoning technologies to the GNSS centric architecture. Refinement of the error model through testing campaigns may lead to achieve results closer to the reality.

### 3.2.6 Test results and analysis

Three different tests have been performed, one for each scenario supported by the statistical channel proposed in the ASTRail project [RD.2]: this analysis, however, will focus on the scenario that exhibits the larger errors due to the local channel effects, i.e. the urban one [RD.2]; finally, results for the suburban and open sky scenarios will be briefly reported.

#### 3.2.6.1 *Performance in urban scenario*

The first test has been performed by analysing the PVT accuracy obtained without the use of the proposed integration algorithm.

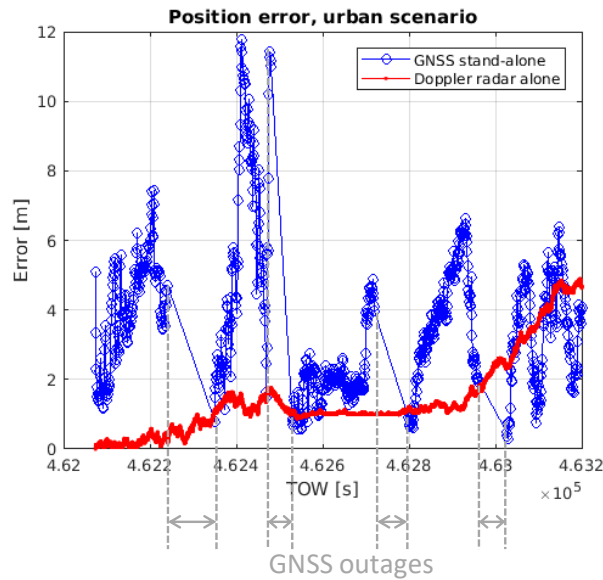


**Figure 11 – Urban scenario, positioning errors without integration algorithm**

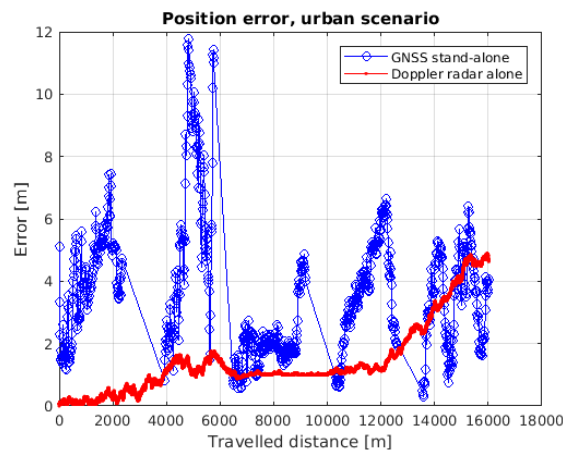


**Figure 12 - Urban scenario, positioning errors without integration algorithm (in function of the travelled distance)**

In Figure 11 and Figure 12, we can see that errors in the GNSS positioning are very large, confirming the need for some kind of mitigation of the local channel effects.

On the contrary, the positioning based on the Doppler radar alone, even if affected by smaller errors, exhibits a growing trend which is typical of the dead-reckoning-based positioning systems. Moreover, it requires an initial estimation of positioning and velocity as accurate as possible. In this simulation this initial condition has been simulated without errors, which could be indicated as an optimistic condition.

The positioning error obtained by using the loosely coupled integration is reported by Figure 13: the error obtained by the loosely coupled integration follows closely the error obtained by the stand-alone GNSS receiver, with some minor improvements. During the GNSS outages, the loosely coupled algorithm is able to continue the PVT estimation while limiting the growth of the error.

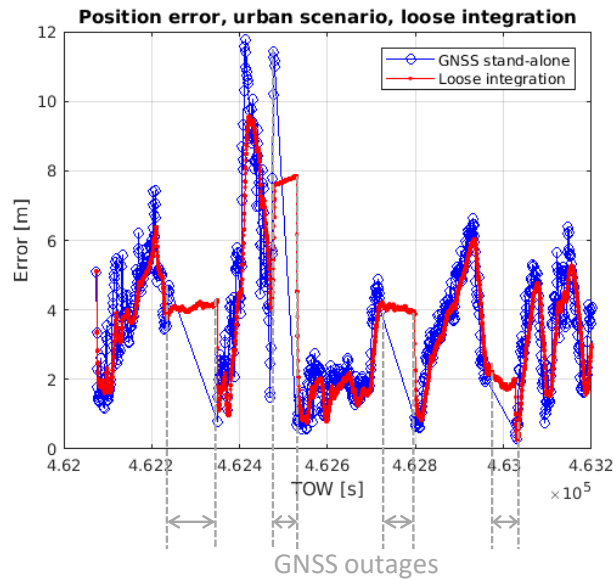


**Figure 13 – Urban scenario, positioning error for GNSS only and loosely coupled integration**

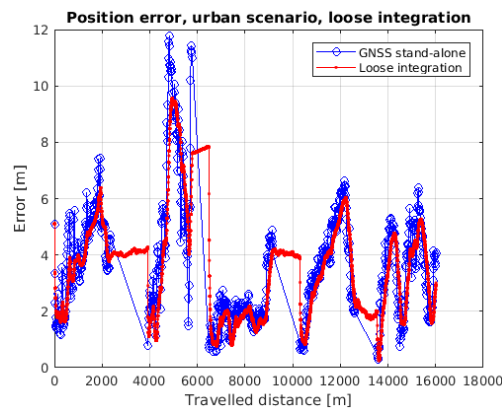


**Figure 14 - Urban scenario, positioning error for GNSS only and loosely coupled integration (in function of the travelled distance)**

Results reported in Figure 13 and Figure 14 show that a careful design of weights used during the integration is required to obtain better performance. The parameters used for this optimization are

- the elements of the covariance matrix of the measurements noise  $\mathbf{R}$  related to the odometer measurements, which weights the available measurements during the update phase of the KF;
- the covariance matrix of the model noise  $\mathbf{Q}$ , which weights predicted states and measurements during the update phase of the KF.

The performance of the loosely coupled integration has been evaluated while changing the values in the  $\mathbf{R}$  matrix: using lower values for the matrix elements related to the odometer measurements,  $R_o$ , the odometer measurements are weighted more than the GNSS measurements during the update phase of the KF. Figure 15 and Table 3 report the positioning errors and their statistics for different choices of  $R_o$ .

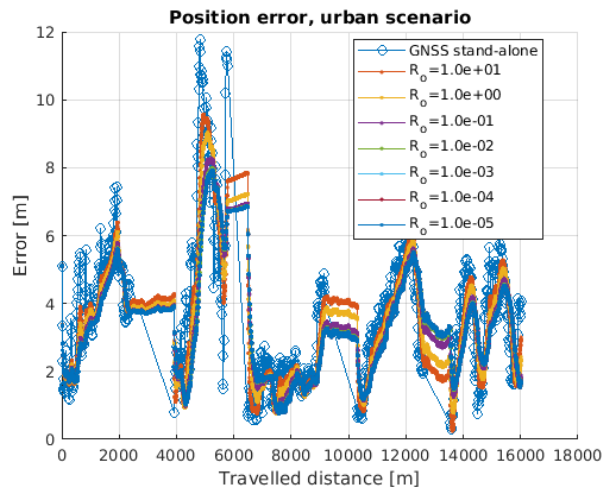


**Figure 15 – Urban scenario, positioning error in function of the R matrix**

Integration	$R_o$	Position error, mean	Position error, std
No, GNSS stand-alone	-	3.69 m	2.10 m
Yes	10	3.42 m	1.95 m
Yes	1	3.35 m	1.86 m
Yes	$10^{-1}$	3.25 m	1.74 m
Yes	$10^{-2}$	3.19 m	1.68 m
Yes	$10^{-3}$	3.18 m	1.66 m
Yes	$10^{-4}$	3.18 m	1.66 m
Yes	$10^{-5}$	3.18 m	1.66 m

**Table 3 - Urban scenario, positioning error statistics in function of R**

Table 3 shows that when  $R_o$  is decreased also the error mean and standard deviation decrease. When  $R_o < 10^{-3}$ , the advantages are negligible, so the value  $R_o = 10^{-3}$  is selected for the following simulations.

Figure 15 shows that the behaviour of the positioning error still closely follows the behaviour of the GNSS stand-alone system. In order to get better performance, the prediction stage of the KF should be weighted more than the measurements: this has been obtained by changing the values of the  $Q$  matrix, namely by inserting a correction factor  $q$  and setting  $Q = qQ_0$  where  $Q_0$  stores the default values. Figure 16 and Table 4 show the obtained results for different choices of  $q$ .

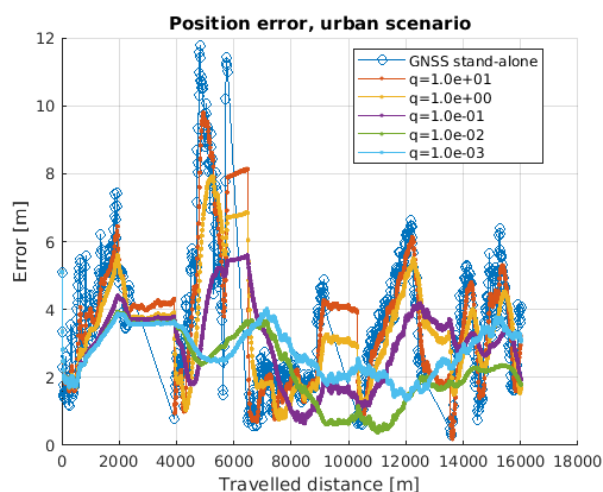


**Figure 16 – Urban scenario, positioning error in function of the Q matrix**

Integration	$q$	Position error, mean	Position error, std
No, GNSS stand-alone	-	3.69 m	2.10 m
Yes	10	3.44 m	1.97 m
Yes	1	3.18 m	1.66 m
Yes	$10^{-1}$	2.81 m	1.13 m
Yes	$10^{-2}$	2.25 m	0.94 m
Yes	$10^{-3}$	2.77 m	0.77 m

**Table 4 - Urban scenario, positioning error statistics in function of Q**

When the values in the  $Q$  matrix is decreased, the prediction is weighted more than the update phase, so the resulting errors depicted in Figure 16 follow the GNSS stand-alone case less closely. Table 4 shows that the best performance in terms of mean value of the errors is reached with  $q = 10^{-2}$ , whereas the standard deviation still decreases with  $q = 10^{-3}$ . For the following simulations,  $q = 10^{-2}$  is selected.

The large initial error reported in Figure 16 is due to the position error in the first PVT estimation from the GNSS receiver. This problem refers to the Position Operation Condition OCP-2 and OCP-3 which are strictly related to the *start of mission* issue (details in [RD.3]). With the available GNSS stand-alone performance, a simple way to decrease the initial error is in the use of balises to obtain a correct initial position. An additional simulation has been conducted by simulating the presence of one balise at the start of the track: the results are shown in Figure 17 and Table 5.

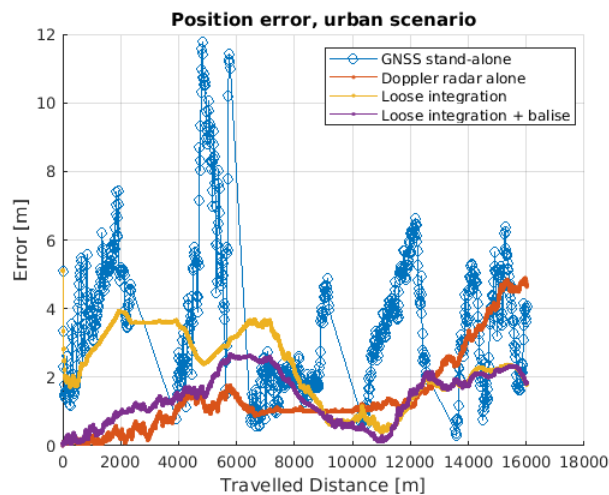


**Figure 17 – Urban scenario, positioning error when using a balise**

Integration	Balise available	Position error, mean	Position error, std
No, GNSS stand-alone	- <sup>1</sup>	3.69 m	2.10 m
No, Doppler radar alone	Yes	1.55 m	1.32 m
Yes	No	2.25 m	0.94 m
Yes	Yes	1.41 m	0.77 m

**Table 5 - Urban scenario, positioning error statistics when using a balise**

Table 5 shows that the best performance are available from the system made by GNSS, Doppler radar, and wheel odometer with the cooperation of a balise: previous projects foresaw the use of balises in conjunction of GNSS and odometer to grant sufficient performance in critical conditions, like the start of the mission [RD.3]. Moreover, in the KF, even if the state model is weighted more than the measurements, the loose integration algorithm is able to reduce the drifting trend that characterizes the Doppler radar alone solution, as it is visible in the right-hand part of Figure 17. Due to the drift that characterizes the dead reckoning solution, longer simulations are expected to lead to an incremented advantage of the integrated solution w.r.t. Doppler radar alone solution.

Finally, in longer simulations the advantages due to the use of a balise should decrease: in Figure 17, after the initial transient, the loose integration solutions with and without the balise exhibit similar performance.

### 3.2.6.2 Performance in suburban scenario

Figure 18 and Table 6 report the positioning errors in the case of a suburban scenario (see Table 2 for details). The comparison is performed between

- the GNSS stand-alone solution;
- the Doppler radar alone solution, with an ideal initial position estimation;
- the loose integration with the weights selected as described in Section 3.2.1 and the initial position provided by a balise.

<sup>1</sup> The GNSS stand-alone receiver does not make use of external positioning information. So, in Table 5, the presence of the balise is flagged 'don't care' in the row related to the GNSS stand-alone case. The same comment stands also for the other tables in the remaining part of this section.

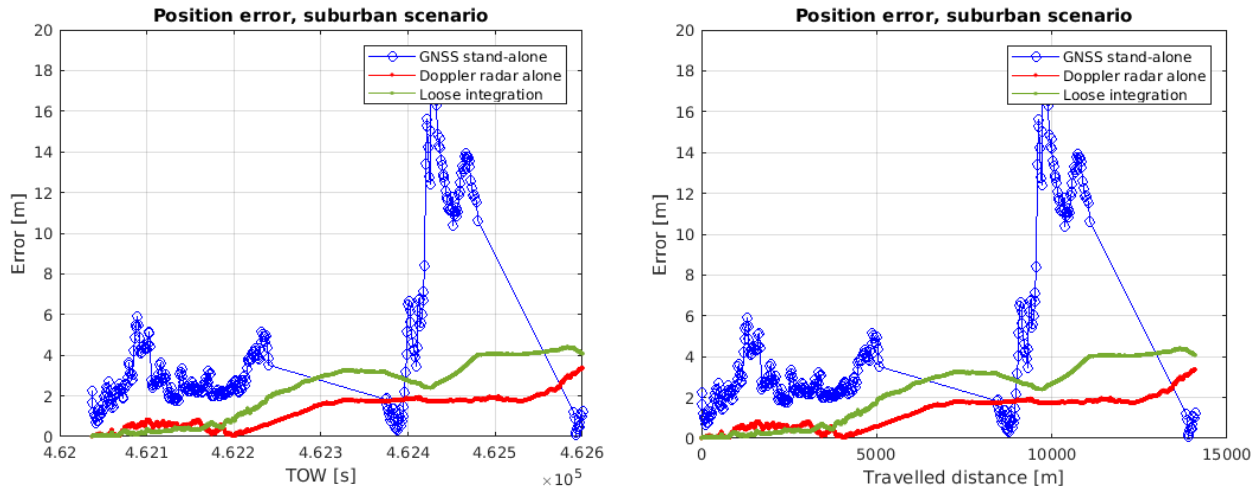


Figure 18 – Suburban scenario, positioning error

Integration	Balise available	Position error, mean	Position error, std
No, GNSS stand-alone	-	4.75 m	4.36 m
No, Doppler radar alone	Yes	0.96 m	0.80 m
Yes	Yes	1.46 m	1.33 m

Table 6 - Suburban scenario, positioning error statistics

In the case of the suburban scenario, the performance of the loose integration is slight worse than the one obtained by the dead reckoning with Doppler radar. It must be noticed that, to reduce the complexity of the channel model generation, the duration of the simulation is reduced w.r.t. the urban scenario (see Table 2): it is expected that, with a longer simulation, the drift of the reckoning solution would lead to an increased positioning error, which results in positioning errors statistics comparable to the ones obtained in the urban scenario

### 3.2.6.3 Performance in open sky scenario

The comparison described in Section 3.2.6.2 is here reported in the case of the open sky scenario (Table 2). Figure 19 and Table 7 provide a plot of the positioning error and the error statistics respectively.

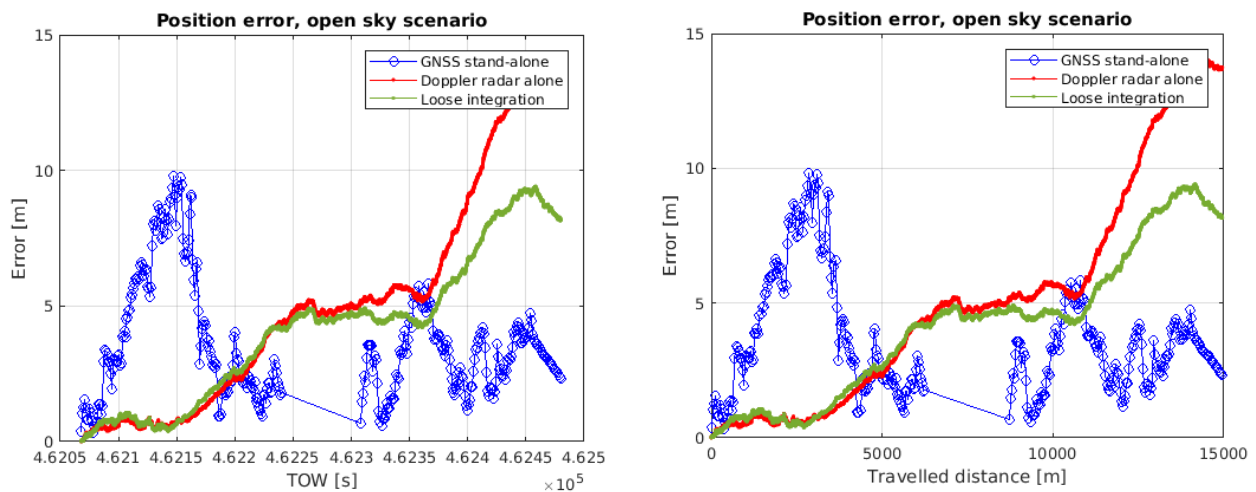


Figure 19 – Open sky scenario, positioning error

Integration	Balise available	Position error, mean	Position error, std
No, GNSS stand-alone	-	3.75 m	2.10 m
No, Doppler radar alone	Yes	5.22 m	4.56 m
Yes	Yes	4.06 m	2.94 m

**Table 7 – Open sky scenario, positioning error statistics**

In the open sky scenario, the dead reckoning solution based on the Doppler radar shows degraded performance w.r.t. the GNSS stand-alone solution. The loose integration is able to limit this behaviour, reaching an intermediate performance level between the two separate solutions.

### 3.2.7 Final remarks

To improve the performance of a GNSS receiver in presence of local channel impairments a loosely coupled integration of GNSS receiver, Doppler radar and wheel odometer has been presented. Its performance have been verified by using the channel model proposed in [RD.2], and the analysis of the results leads to the following general conclusions:

- the integration of Doppler radar and odometer is needed to cope with outages of the GNSS signal, when the GNSS receiver is no more able to provide PVT results;
- the integration of Doppler radar and odometer greatly helps to limit the positioning errors which affect the GNSS receiver;
- the use of GNSS helps to prevent the drifting of the position which characterizes the dead reckoning system when the position is got from the use of the Doppler radar alone;
- the balise is much useful to limit the positioning errors in the *start of mission* conditions.

The amount of the advantage of the integrated solution w.r.t. the separated GNSS and dead reckoning solutions depends on the considered scenario: the characteristics of the dead reckoning system play a major role in this behaviour. Figure 20 shows how the error of the positioning based on the Doppler radar alone changes in function of the simulated train velocity, i.e. with the simulated scenario: the higher is the train velocity, the larger and faster is the increment of the positioning error. Based on this results, a further development of the algorithm could be a velocity-based initialization of the KF matrices  $R$  and  $Q$ :

- when the velocity is low, the Doppler radar drift is lower and the GNSS receiver is seriously impaired by the effects of the local channel, so values of  $R$  and  $Q$  that increase the weight of Doppler radar and wheel odometer should be chosen;
- when the velocity is high, the dead reckoning system drifts quickly and the GNSS receiver is less affected by the local channel effects, so the weights of the GNSS measurements should be increased w.r.t. the odometer measurements ( $R$ ) and the Doppler radar based predictions ( $Q$ ).

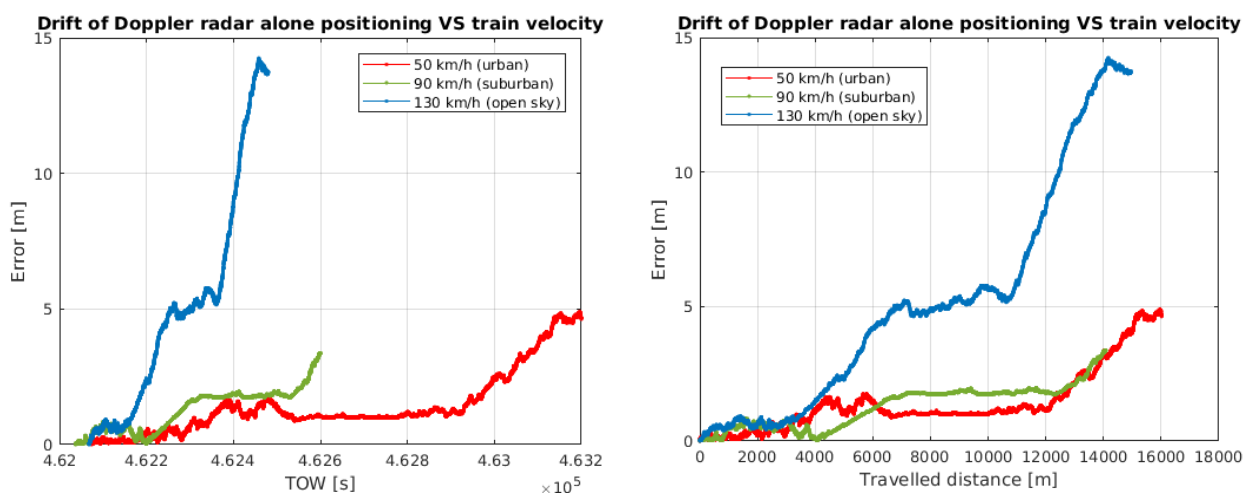


**Figure 20 – Dead reckoning positioning error in function of the train velocity**

Finally, some improvements can be devised to enhance the results presented in this document:



- The use of an RF GNSS signal generator that directly supports the generation of a proper multipath propagation channel model would enable longer simulation than the software model used here, where the statistical model LMSCM limits the duration of the tests and the employed signal generator limits the number of simulated reflected rays. It must be noticed that longer simulation helps to emphasize the effects due to the drifting of the dead reckoning positioning systems.
- The use of more sophisticated GNSS based positioning solutions (e.g. RTK) could grant better performance from the GNSS receiver and then reduce the need for a balise in the *start of mission* condition. To test this case an RF signal generator able to simulate required correction must be employed. Moreover, a better quality of the GNSS positioning could help to reduce the weight of the complementary system inside the loose integration.

## 4 Algorithms for enhanced robustness against RFI: performance analysis

The contents of this section are part of two published papers:

1. **M. Troglia Gamba and E. Falletti. Performance Analysis of FLL Schemes to Track Swept Jammers in an Adaptive Notch Filter. In Proceedings of NAVITEC 2018, ESA-ESTEC, Noordwijk, The Netherlands, 5-7 December 2018**
2. **W. Qin, M. Troglia Gamba, E. Falletti and F. Dosis. A Comparison of Optimized Mitigation Techniques for Swept-frequency Jammers. In Proceedings of the 2019 International Technical Meeting of The Institute of Navigation (ION-ITM) 2019, Hyatt Regency Reston Reston, Virginia, 28 – 31 January 2019**

As detailed in [RD.3], the Adaptive Notch Filter (ANF) has been selected as a viable candidate for the RFI detection and mitigation to be adopted in a GNSS-centric architecture for the railways domain. In particular, a specific family of ANFs has been identified, namely the Frequency Lock Loop (FLL) – equivalent ANFs. Two are the FLL models considered: the standard FLL and the FLL with exponential filtering.

In this section, the performance evaluation of the two FLL models is reported. In particular, the subsection 4.1 illustrates the analysis of their tracking capability and noise performance in absence of the GNSS signal, while subsection 4.2 assesses their filtering efficiency in the first stage of a GNSS receiver.

### 4.1 Tracking capability and noise performance analysis

In this subsection, simulation results obtained according to the methodology of analysis described in [RD.3] are presented. In particular, two are the considered performance indicators:

1. the *dynamic stress error*, defined as the frequency estimation error in the absence of noise, with an input signal in the form defined in Table 8;
2. the *noise jitter*, defined as the frequency estimation error expressly due to the presence of additive noise entering in the estimation loop and independent from the input signal component.

While the former assesses the ANFs' tracking capability, the latter measures their capability of discriminating the interfering signal from the noise. No GNSS signal has been considered for this first test campaign. For a detailed description of above mentioned key performance indicators as well as of the two adopted FLL models of ANF, please refer to [RD.3].

Chirp Type	Jammer Name	Jammer features			
		Rate	Sweep range (MHz) ( $f_{min}, f_{max}$ )	Sweep period $T_{chirp}$ (μs)	Sweep rate $\beta_f$ (MHz/μs)
Linear	Wide sweep	slow	(-8, 8)	33	0.48
		medium		20	0.8
		fast		10	1.6

Chirp Type	Jammer Name	Jammer features			
		Rate	Sweep range (MHz)	Sweep period $T_{chirp}$ (μs)	Sweep rate $\beta_f$ (MHz/μs)
			$(f_{min}, f_{max})$		
		rapid		6.25	2.56
Triangular	Triangular wave	--	(-7, 7)	20	1.4

**Table 8 – Main features of the selected jammers, as reported in [RD.3].**

Subsections 4.1.1 and 4.1.2 are devoted to the dynamic stress response analysis in the presence of the two jamming signals in Table 8. Subsection 4.1.3 is devoted to the evaluation of the noise performance.

Since the addressed performance are only marginally dependent on the pole contraction factor, it is considered constant for all the performed tests:  $k_\alpha = 0.95$ , resulting in a feasible notch rejection bandwidth  $B_{3dB} \approx \frac{(1-k_\alpha)\pi}{10} f_s = 628$  kHz.

#### 4.1.1 Linear chirp-response evaluation

For a linear chirp signal, the instantaneous frequency can be written as

$$f_J[n] = f_{min} + \beta_f \cdot \text{rem}(n, L_c) \quad (21)$$

where ‘rem’ is the remainder of the integer division between  $n$  and  $L_c$ ,  $L_c = \left\lfloor \frac{T_{chirp}}{T_s} \right\rfloor$ ,  $\beta_f$  is the sweep rate, or chirpiness, defined in Table 8. Hereafter, the wide sweep-slow jammer with  $T_{chirp} = 33 \mu\text{s}$  has been considered.

Figure 21 reports the steady state error (a), the settling time (b) and the maximum overshoot (c) as a function of  $B_n$  for the first-, second- and third-order loop in the standard FLL. It can be observed that both the steady-state error and settling time reduce when  $B_n$  increases, as expected, while the overshoot in Figure 21-(c) follows the opposite trend, at least for the second- and third-order loops, as a reaction to the signal discontinuities. No overshoot is shown by the first-order loop for all the considered values of  $B_n$ , as expected. As a general observation, the filter become more and more responsive to the input dynamics for higher  $B_n$  and higher orders. Indeed, the overshoot also grows with  $K$ , thus affecting the settling time with a slight increase for higher filter orders.

Figure 21-(b) also indicates the duration of the chip period  $T_{chirp}$  with the black dashed line: if we consider acceptable a settling time lower than at least 10% of the chirp period, i.e.  $t_{set}^{max} = 10\% T_{chirp} = 3 \mu\text{s}$  for the considered case (see the grey dotted line), then we see that the second- and third-order loops achieve the target with  $B_n$  greater than approximately 4 MHz; on the other hand, although the settling time of the first-order loop is acceptable for loop bandwidths from 0.8 MHz on, the corresponding steady-state error is not so satisfactory if compared with the higher orders (Figure 21-(a)). Finally, the second- and third-order loops in Figure 21-(a) are able to achieve the lower bound of their frequency estimation capability, which can be expressed by

$$e_{LB} = \frac{\beta_f T_s}{2} = \frac{1}{2} \frac{\Delta f}{T_{chirp}} T_s \quad (22)$$

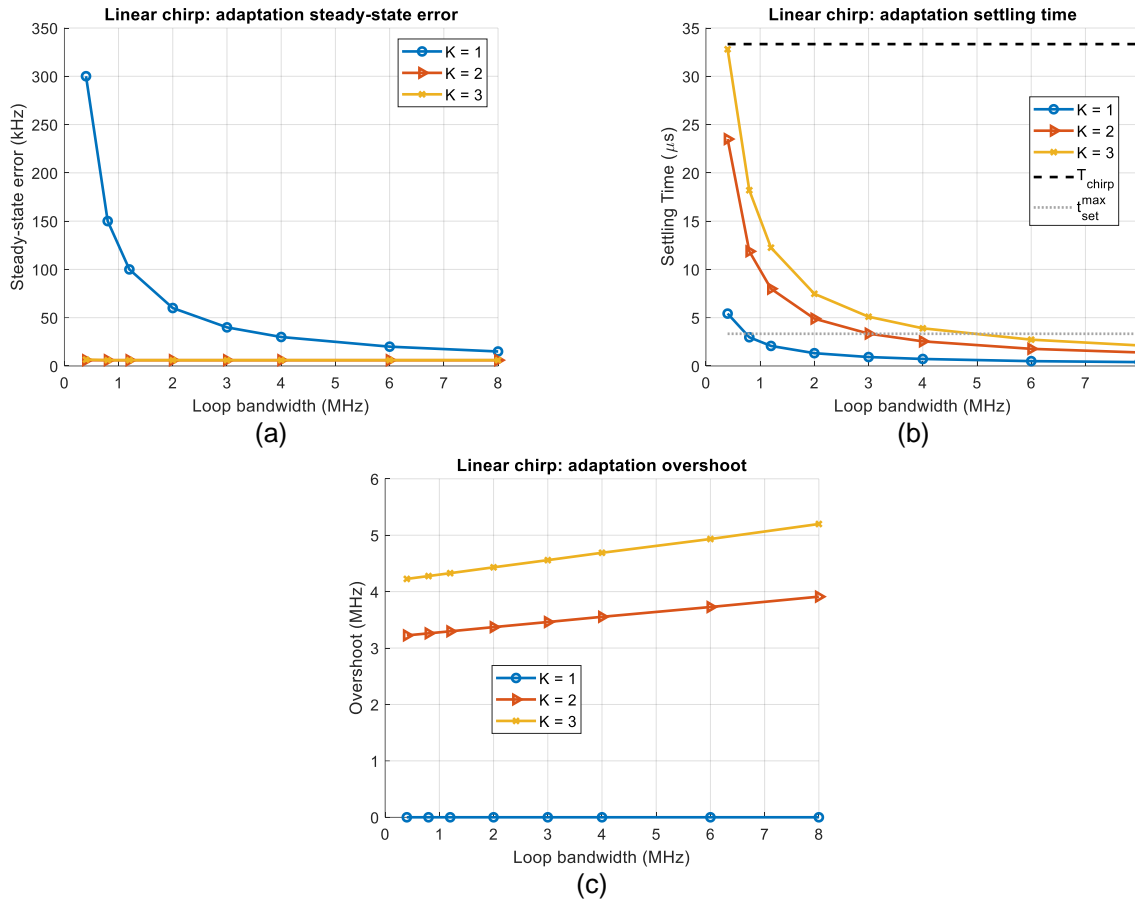


**Figure 21 –Standard FLL adaptive block response to linear chirp: steady-state error (a), settling time (b) and overshoot (c) evaluation as a function of the loop bandwidth  $B_n$ , for constant pole contraction factor and sampling frequency,  $k_\alpha = 0.95$  and  $f_s = 40$  MHz. Curves are parameterized on the filter order  $K$ .**

Clearly, the lower-bound values  $e_{LB}$  increase with the sweep rate  $\beta_f$  and reduce with increasing the sampling frequency  $1/T_s$ . This behavior is quantified in Figure 22 for various values of sampling frequency and the sweep rates of Table 8.

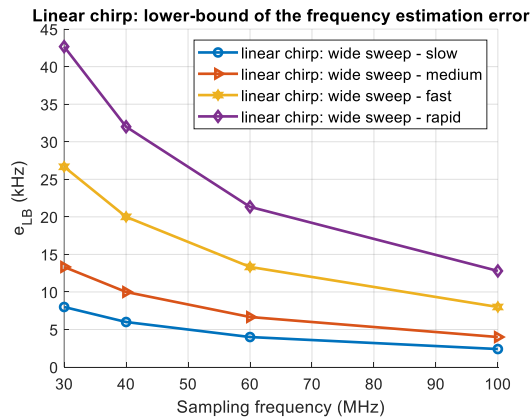


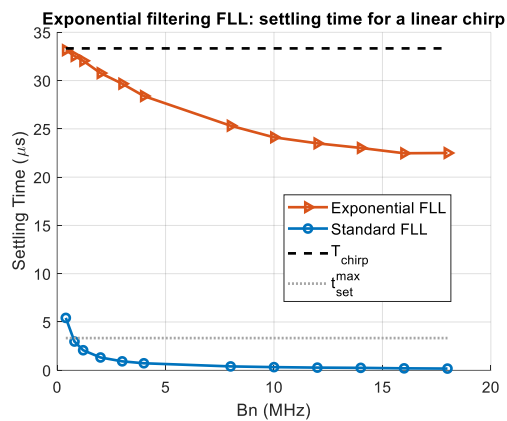
**Figure 22 – Lower bound of the frequency estimation error,  $e_{LB}$ , as a function of the sampling frequency. Curves are parameterized on the sweep rate.**

#### 4.1.1.1 Standard FLL vs exponential filtering FLL

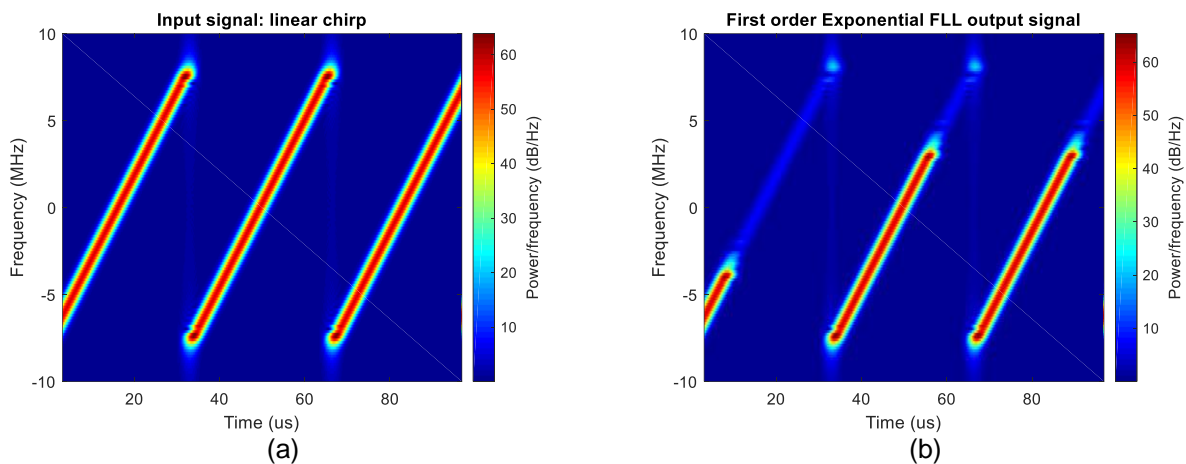
Although we expect much degraded performance for the exponential FLL in the presence of the interfering signals of Table 8, as mentioned in [RD.3], we complete here the discussion of the linear chirp response with

a comparison between the first-order exponential [16][17] and the first-order standard FLLs in terms of settling time, for different values of the loop bandwidth  $B_n$ , computed as a function of  $\mu_0$  and  $k_\alpha$  [17]. Figure 23 shows that, for the selected  $k_\alpha = 0.95$ , the gap between the exponential filtering FLL (red plot with triangle markers) and the standard FLL (blue plot with circle markers) is quite significant. Indeed, while the exponential FLL spends more than 65% of the sweep period to converge to the correct frequency, the standard FLL takes less than 10% for loop bandwidths from 0.8 MHz on, as already shown in Figure 21-(b). This confirms the limitations of the exponential FLL adaptation algorithm in the conditions of interest. It is worth noticing that in the exponential filtering FLL the pole contraction factor not only controls the notch rejection bandwidth, but also determines the decay rate of the exponential filter and therefore the loop bandwidth: the bigger  $k_\alpha$ , the smaller the notch bandwidth, but the slower the filter will be.

The different tracking capabilities of the two adaptive algorithms are further demonstrated by the spectrogram evaluation in Figure 24. Three chirp periods of the wide sweep-slow jammer are plotted, using 256 FFT points. The input signal is shown in Figure 24-(a), while in Figure 24-(b) the output of the exponential filtering FLL ANF is reported: from the second chirp period on, it is able to filter only the final upper frequencies of the jammer, making it not effective for such kind of interfering signals. The better performance of the standard FLL compared to the exponential filtering FLL (order  $K = 1$ ) are further confirmed in Figure 24 (c), where the jammer is considerably filtered out. Finally, for  $K = 2$  the standard FLL is able to remove it almost completely: only a few energy in the lower frequencies still remains, corresponding to the transient time of the FLL response.



**Figure 23 –Settling time evaluation as a function of the loop bandwidth  $B_n$  for the first-order exponential FLL and the first-order standard FLL ANFs, for constant pole contraction factor and sampling frequency,  $k_\alpha = 0.95$  and  $f_s = 40$  MHz.**



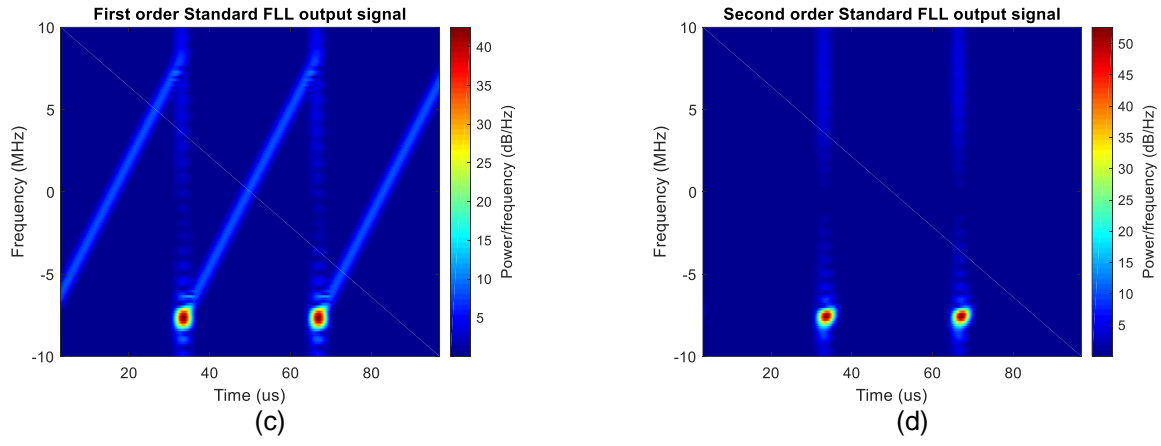


**Figure 24 –ANF response to slow linear chirp: spectrogram evaluation of the input signal (a) and outputs of the exponential filtering FLL ANF (first-order loop) (a) and standard FLL ANF with loop order  $K = 1$  (b) and  $K = 2$  (c) . The loop bandwidth has be set to  $B_n = 3$  MHz.**

#### 4.1.2 Triangular chirp-response evaluation

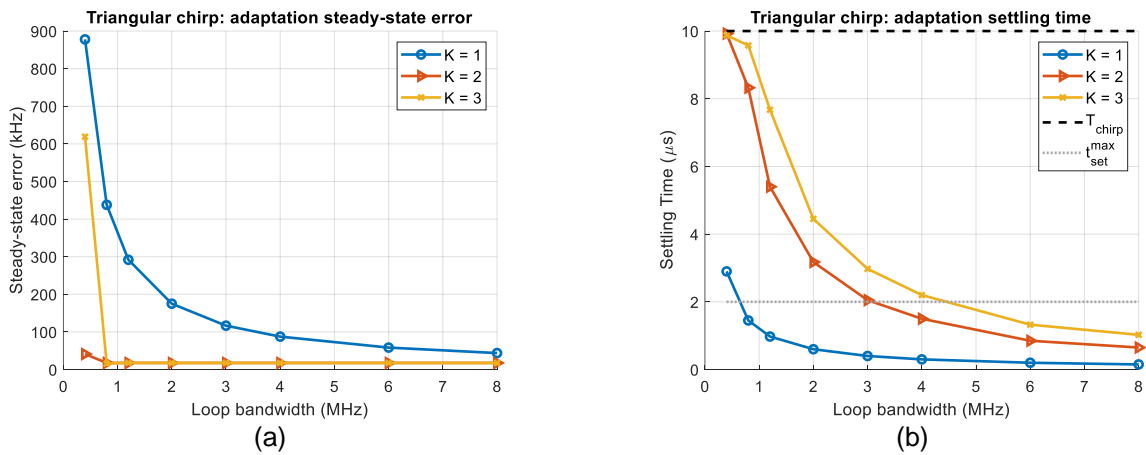
The dynamic stress response analysis performed in the previous subsection is hereafter repeated for the triangular wave included in Table 8. In this case, the instantaneous frequency can be written as:

$$f_f[n] = \begin{cases} f_{min} + \beta_f \cdot \tilde{n}, & \tilde{n} \leq \left\lfloor \frac{L_c}{2} \right\rfloor \\ (f_{min} + 2\Delta f) - \beta_f \cdot \tilde{n}, & \left\lfloor \frac{L_c}{2} \right\rfloor < \tilde{n} < L_c \end{cases} \quad (23)$$

where  $\tilde{n} = \text{rem}(n, L_c)$ .

The evaluated metrics are shown in Figure 25 for the standard FLL. Similar to the linear chirp case, the steady-state error and the settling time in Figure 25-(a) and (b) decrease when  $B_n$  increases. Second-and third-order loops outperform the first-order one in terms of steady-state error, and both reach the lower bound  $e_{LB}$  for  $B_n \geq 2$  MHz. Opposite to the linear-chirp case, the overshoot Figure 25-(c) reduces with  $B_n$ : this can be most likely explained by the frequency continuity of the triangular wave jammer, with no jumps. The trend with  $K$  still is the same as in Figure 21-(c).

Since no frequency discontinuities are present in the jamming signal, the exponential filtering FLL behaves in a better way, but still far from the performance of the standard FLL. It is able to track the triangular chirp for loop bandwidths from 3 MHz on. Being not significant, results are not shown.



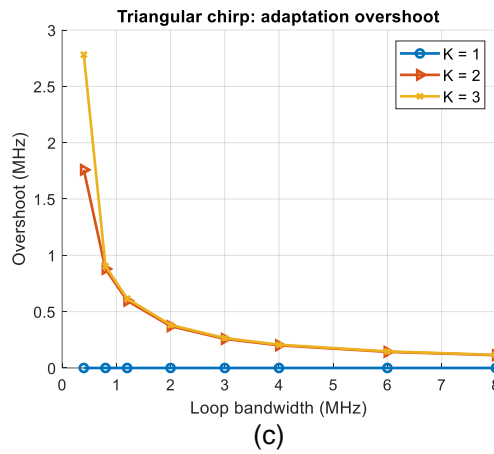


**Figure 25 –Standard FLL adaptive block response to triangular chirp: steady-state error (a), settling time (b) and overshoot (c) evaluation as a function of the loop bandwidth  $B_n$ , for constant pole contraction factor and sampling frequency,  $k_\alpha = 0.95$  and  $f_s = 40$  MHz. Curves are parameterized on the filter order  $K$ .**

#### 4.1.3 Frequency jitter evaluation

In this subsection the standard FLL adaptation block is analyzed in the presence of noise. Figure 26 reports the standard deviation of the frequency jitter estimated for different Interference-to-Noise Ratio (INR) values and filter orders. Without loss of generality, the figure reports only two values of loop bandwidths,  $B_n = \{3, 6\}$  MHz, and the linear chirp model, but the same observations can be done for other values of  $B_n$  and input characteristics. While the error contribution due to the type and rate of the jamming signal is in the order of kHz, as shown in Figure 21, Figure 22 and Figure 25, the noise contribution can reach even the MHz for low INRs, also reducing the gap between  $K = 1$  and  $K = \{2, 3\}$ , although the advantage of second- and third-orders over the first one still is evident.

As expected, the frequency jitter reduces for lower  $B_n$ , since less noise is entering the system, depending on the INR: for high noise conditions, i.e. low INR, using a smaller  $B_n$  allows to reduce the jitter up to 40 %, thus removing the jamming signal with a better accuracy. As already mentioned, higher loop orders achieve better performance, with a small advantage of the third-order over the second- one. This result is in line with the one obtained in subsections 4.1.1 and 4.1.2.

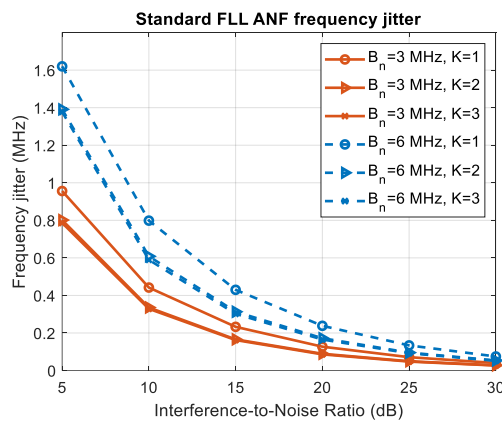


**Figure 26 – Estimated noise jitter for the standard FLL, for loop bandwidth  $B_n = \{3, 6\}$  MHz, filter order  $K = \{1, 2, 3\}$  and a linear chirp – wide sweep-slow. Constant pole contraction factor and sampling frequency,  $k_\alpha = 0.95$  and  $f_s = 40$  MHz, are considered.**

## 4.2 Filtering efficiency analysis in a GNSS receiver

In this subsection, the performance comparison between the standard and exponential FLL ANFs in terms of filtering efficiency in the first stage of a GNSS receiver is presented. In particular, subsection 4.2.1 reports the adopted methodology, while the achieved results are shown in subsection 4.2.2.

### 4.2.1 Methodology for performance evaluation

In a GNSS receiver, the filtering efficiency as well as distortion effects of ANFs can be assessed considering different key performance indicators along the whole GNSS signal processing chain. The first indicator of the ranging code distortion is the  $\alpha_{mean}$  measured at the GNSS signal acquisition stage. In fact, it is well known that the jammers aim at blinding the GNSS receivers and blocking the acquisition stage. It is then important that any mitigation techniques not only remove the spurious power of the interference, but also improve as much as possible the detection probability of the GNSS signals by the receiver.

In acquisition, the incoming signal is correlated with a series of locally generated replicas until the acquisition detector crosses a predefined threshold, i.e. a correlation peak has been found in the search space. Based on this, the impact of interference on the acquisition stage can be evaluated by exploiting a figure of merit, namely  $\alpha_{mean}$ , which is defined in [18] as the correlation peak-to-noise-floor ratio, given by

$$\alpha_{mean} = 20 \log_{10} \left( \frac{x_p}{E_i} \right) \quad (24)$$

where  $x_p$  is the correlation peak at the acquisition stage and  $E_i$  is the average of  $i$  off-peak correlation points in the acquisition search space.

As the interfering power increases, the value of  $\alpha_{mean}$  decreases thus leading to an increasing probability of a false alarm [18]. When the ANF is adopted to mitigate the interference, e.g. jamming signals, the  $\alpha_{mean}$  values can also be used to evaluate its filtering efficiency with different parameter settings at the acquisition stage. The parameter settings of ANF should be carefully tuned in order to enable the filter to successfully track and mitigate the jamming signals.

As exemplary case, Figure 27 shows the Cross-Ambiguity Function (CAF) of the input signal at the acquisition stage in case of a strong jamming interference. In particular, the CAF of the unfiltered signal is reported in Figure 27-(a), while the one of the filtered signal is illustrated in Figure 27-(b). Due to the strong interference, the power of the interference is distributed on the whole search domain in Figure 27-(a), leading to a failure in the acquisition with  $\alpha_{mean} = 21.6 \text{ dB}$ . After interference mitigation with a good combination of parameters achieved through the previous analysis, the acquisition is achieved with  $\alpha_{mean} = 37.8 \text{ dB}$  as shown in Figure 27-(b).

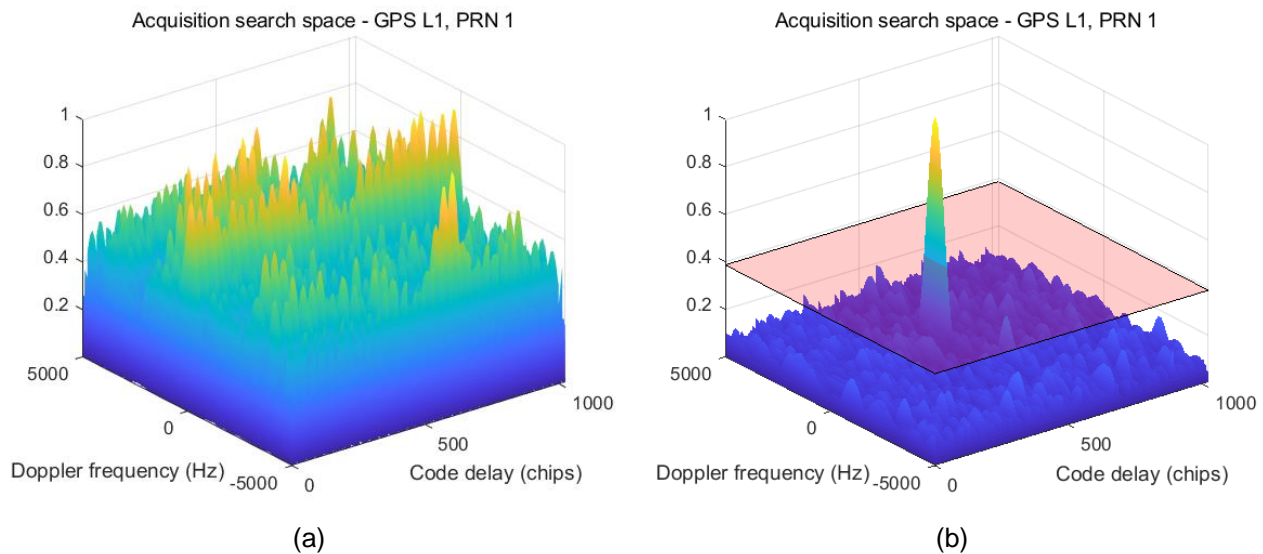




**Figure 27 – CAF of the interfered signal before (a) and after (b) the interference mitigation.**

#### 4.2.2 Performance evaluation

Hereafter, the filtering efficiency analysis, introduced in the previous subsection on the basis of the  $\alpha_{mean}$  parameter, is performed for several values of Jammer-to-Noise ratio and Jammer-to-Signal conditions.

The performance evaluation tests are conducted via simulation. The GPS L1 signal is generated by the N-FUELS Signal Generation Tool [19][20] at baseband with a sampling rate of 40 MHz. Only one GPS satellite has been simulated. In addition, an 8<sup>th</sup> order Butterworth Front-End (FE) filter, with 20.46 MHz pass-band is employed, while no Analog-to-Digital Converter (ADC) is adopted to intentionally preserve the signal full dynamic with no quantization losses. The signal and noise density powers are set respectively to  $P_C = -146.3$  dBW and  $N_0 = -201.3$  dBW/Hz, resulting in a carrier to noise ratio  $C/N_0$  of 55 dB-Hz. A wide-sweep slow rate jamming signal, whose features are reported in Table 8, is then added to the baseband complex envelope of the clean signal: three jamming powers  $P_J = \{-130, -110, -103\}$  dBW are considered to simulate respectively a weak, medium and strong jammer scenarios, resulting in  $J/N = \{-1.8, 18.2, 25.2\}$  dB and  $J/S = \{16.3, 36.3, 43.3\}$  dB.

The generated signal is given as input to the MATLAB® model of the FLL-equivalent ANFs. The filtered signal is finally processed by a MATLAB®-based GNSS software receiver, where only the acquisition stage is enabled. An FFT-based Parallel Code Phase Search Acquisition is adopted, with integration time  $T_{int} = 1$  ms, one coherent/non-coherent sums and false alarm probability  $P_{fa} = 0.001$ . The  $\alpha_{mean}$  metric is evaluated according to (24) and averaged along 50 ms total signal length.

Figure 28 reports the  $\alpha_{mean}$  evaluation for the three considered jamming scenarios for both the exponential filtering FLL (Figure 28-(a), (c) and (e)) and the standard FLL (Figure 28-(b), (d) and (f)). In particular, the top subplot shows  $\alpha_{mean}$  as a function of the pole contraction factor  $k_\alpha$  and the loop bandwidth  $B_n$ , while the bottom one illustrates the successful acquisition percentage  $\gamma$ , defined as the total percentage of time in which the signal has been successfully acquired. The grey dashed line and grey bars are used for the unfiltered signal (ANF disabled), as reference, while all other colors represent the filtered signal (one color per loop bandwidth  $B_n$ ). For the readers' convenience, the best combination of  $k_\alpha$  and  $B_n$ , i.e. the one achieving the maximum  $\alpha_{mean}$ , is reported. A summary of the performance comparison is also shown in Table 9, where  $\alpha_{mean}$  measurements in case of the filtered signal, using the best parameters setup of the FLL-equivalent ANFs, are evaluated against the unfiltered case for the three  $J/N$  conditions mentioned above. In particular, the third row in Table 9 lists the  $\alpha_{mean}$  when the ANF is disabled, while the fourth and fifth rows contain those achieved with exponential FLL and standard FLL respectively. For both algorithms the percentage improvement with respect to the unfiltered case is also indicated in brackets.

As shown in Figure 28-(a) and (b), the filtering is not really necessary in case of weak jamming power, as expected. Indeed, as clearly pointed out by the grey bars in the bottom plots of Figure 28-(a) and (b), the GNSS signal is always successfully acquired even when the ANF is disabled. The ANF effectiveness become evident when a significant increase of  $\alpha_{mean}$  with respect to the unfiltered case can be measured. In this regard, the exponential FLL shows to be effective for  $0.7 < k_\alpha < 0.9$  and  $B_n > 6$  MHz with a maximum improvement of 1.92 dB (4.4 % in Table 9) for the best parameters combination, i.e.  $k_\alpha^{best} = 0.8$  and  $B_n^{best} = 12$  MHz. On the contrary, the standard FLL cannot be considered really effective. Anyway, for the best parameters choice, i.e.  $k_\alpha^{best} = 0.9$  and  $B_n^{best} = 4$  MHz, performances are comparable with those when the ANF is disabled, with a negligible  $\alpha_{mean}$  degradation (-0.6 % in Table 9).

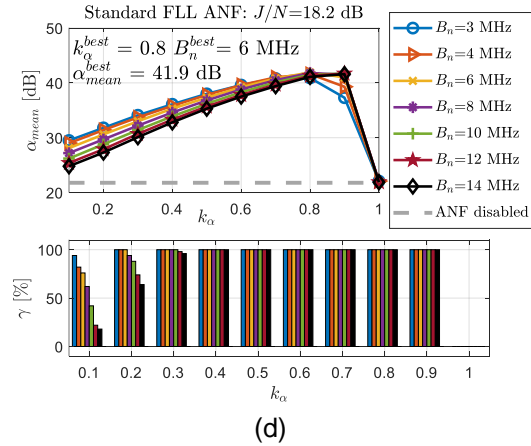
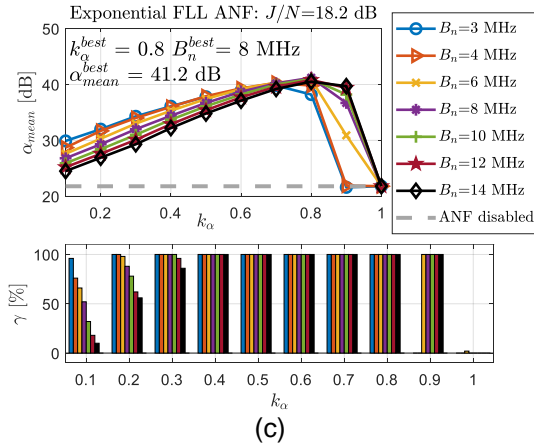
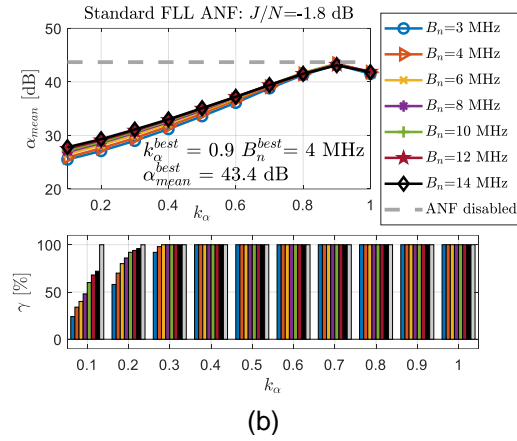
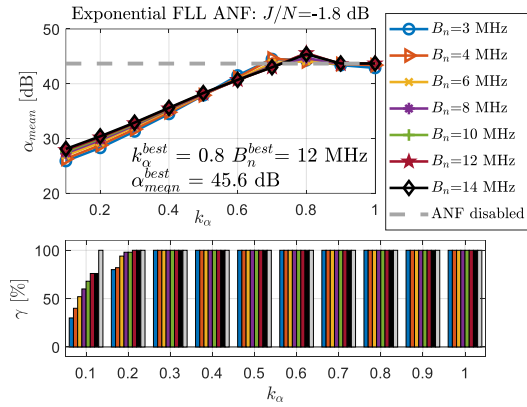
A remarkable  $\alpha_{mean}$  improvement is instead observed for medium and strong jamming powers, as clearly appears in Figure 28-(c), (d), (e) and (f). In all these cases, the ANF is fundamental. Without it, the acquisition is almost impossible, as shown in the bar graphs. The colored bars clearly show a slight reduction of the useful  $k_\alpha$  range for an increasing jamming power. Focusing on the worst case, i.e.  $J/N = 25.2$  dB in Figure 28-(e) and (f), optimal  $\gamma$  are obtained for all the considered loop bandwidths when  $k_\alpha$  is in the range  $[0.5 - 0.8]$ . On the other hand, since the notch rejection bandwidth  $B_{3dB} \approx (1 - k_\alpha)f_s/\pi$  [21], small values of  $k_\alpha$  are not recommended, in order to keep the notch bandwidth as narrow as possible, thus preserving the useful GNSS signal.



In Table 9 the standard FLL overcomes the exponential FLL for medium-strong jammer with about 3 % and 6 % advantage, while showing a 5 % degradation for weak jamming signal. While the former situation finds explanation in the faster reactivity of the standard FLL to the frequency discontinuities produced by the jammer, as pointed out in section 4.1, the latter has to be likely searched in the adaptation rule. Minimizing the Moving Average (MA) output provides a better tracking performance at the price of reducing the capability of discriminating the interference signal from the useful one: this becomes particularly relevant for lower  $J/N$  situations.

According to the above analysis, all these results clearly demonstrate that the pole contraction factor is the only parameter having a significant impact on the  $\alpha_{mean}$  metric, while the loop bandwidth does not have a noteworthy effect. This could be partly explained by the objective of the acquisition stage: a rough estimation of the code delay and Doppler frequency. More relevant differences are expected in the tracking stage, where such estimation has to be refined in order to lock the GNSS signal.

Accepting a small degradation for low  $J/N$  conditions,  $k_\alpha = 0.8$  seems to be a good choice for both the FLL models, while  $4 \text{ MHz} \leq B_n \leq 6 \text{ MHz}$  and  $8 \text{ MHz} \leq B_n \leq 12 \text{ MHz}$  are recommended for the standard FLL and the exponential FLL respectively. This further supports the findings in section 4.1: the standard FLL requires smaller loop bandwidths, thus implying less noise entering the system and consequently lower frequency jitter (standard deviation of the notch frequency error).



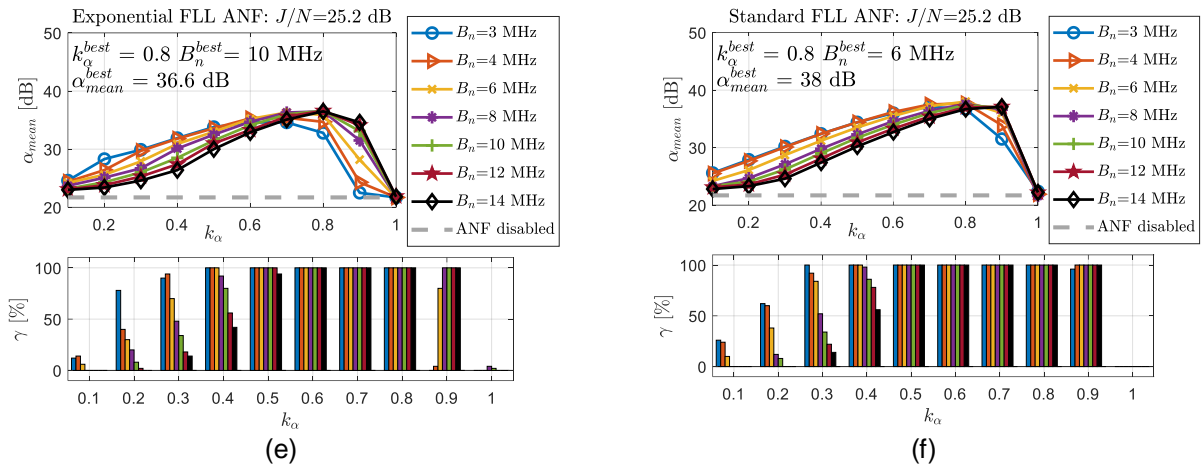


**Figure 28 –  $\alpha_{mean}$  and successful acquisition percentage  $\gamma$  evaluated as a function of the pole contraction factor  $k_\alpha$  and the loop bandwidth  $B_n$  for the standard FLL and the exponential FLL ANFs respectively in case of  $J/N = -1.8$  dB (a)(b),  $J/N = 18.2$  dB (c)(d) and  $J/N = 25.2$  dB (e)(f). Constant  $C/N_0 = 55$  dB – Hz is considered.**

FLL-equivalent ANFs		$J/N$ (dB)		
		-1.8	18.2	25.2
ANF disabled	$\alpha_{mean}$ (dB):	43.68	21.79	21.7
Exponential FLL with best $(k_\alpha, B_n)$ combination	$\alpha_{mean}$ (dB): (% gain)	45.6 (4.4 %)	41.2 (89.1 %)	36.6 (68.7 %)
Standard FLL with best $(k_\alpha, B_n)$ combination	$\alpha_{mean}$ (dB): (% gain)	43.4 (-0.6 %)	41.9 (92.3 %)	38 (75.1 %)

**Table 9 – Comparison of  $\alpha_{mean}$  measured for the signal filtered, using the FLL-equivalent ANFs with the best parameter settings, against the unfiltered case for several  $J/N$  conditions.**

#### 4.3 Final remarks

From the above conducted analysis, we can state that while the standard FLL shows to be able to successfully track and mitigates jamming interferes, the exponential filtering FLL proves to not being able to, suffering particularly from frequency discontinuities, as in case of linear chirps. For this reason, the standard FLL approach is preferred as most suitable solution to enhance the GNSS robustness against RFIs.

## 5 Conclusions

This document presented the performance evaluation of multiple algorithms which have been addressed within ASTRail T1.7. This includes an architecture to diagnose GNSS failures using odometry sensors between physical balises and the enhancement of the positioning solution availability, assessed in section 3. Furthermore, the robustness against RFI has been investigated in section 4.

In particular, the methodology of diagnosis of GNSS faults for train positioning system by utilizing embedded odometry and track geometry has followed multiple steps. The definitions of hazard suitable for GNSS based positioning system for train have been suggested through considering the nature of GNSS faults. The diagnosis scheme comparing measurements of odometry and track geometry with position of GNSS has been provided. Simulations were performed to investigate the effect of choice on GNSS constellation and the advantage of utilizing track geometry information. The simulation results are analyzed in not only probabilistic manner but also in the time domain. The results show that the dual-constellation of GPS and Galileo is beneficial to secure sufficient margin of the detection time from the occurrence of position failure. The usage of track geometry improves consistency of the detection on the placement of faulty satellite or heading change of train.

To enhance the PVT availability in presence of local channel impairments, a loosely coupled integration of GNSS receiver, Doppler radar and wheel odometer has been presented. The performed tests demonstrated the advantages of the data fusion, overcoming the limitations shown by each technology alone. Finally, a performance comparison of two FLL-equivalent ANFs in case of jamming signals has been presented. The two algorithms have been evaluated in terms of tracking capability of the jammer frequency variations, noise jitter and filtering efficiency in a GNSS receiver.

The possible implementation of the proposed algorithms, namely the GNSS hybridization with complementary technology and RFI detection and mitigation, in the VB GNSS-based architecture presented in [RD.3] and recalled in section 2 deserves some more deep insights. In this regard, the proposed RFI detection and mitigation algorithms don't require any modification of the outlined architecture, thus being completely compatible with it. In fact, they represent additional capabilities to be provided by the GNSS receiver.

Similarly, in the GNSS hybridization, the integration scheme is an additional feature to be inserted in the GNSS receiver, but the complementary technologies could have an impact depending on the selected ones, whether or not they are already available on-board the train, and if they are able to meet the requirements. The presented solution has to be considered as an initial study with the main goal of evaluating its feasibility and possible benefits for the railway domain. Its compatibility and practical implementation into the VB GNSS-based architecture has to be verified in the next future.

## 6 Acronyms

Acronym	Explanation
GNSS	Global Navigation Satellite Systems
RFI	Radio-Frequency Interference
S2R	Shift2Rail
IP2	Innovation Programme 2
ERTMS	European Rail Traffic Management System
ETCS	European Train Control System
VB	Virtual Balise
PB	Physical Balise
LU	Localization Unit
EWMA	Exponential Weighted Moving Average
SBAS	Satellite-based Augmentation System
CW	Clockwise
CCW	Counter-clockwise
RTK	Real-time Kinematic
PVT	Position Velocity and Time
KF	Kalman Filter
ANF	Adaptive Notch Filter
FLL	Frequency Lock Loop
CAF	Cross-Ambiguity Function
FE	Front-End
ADC	Analog-to-Digital Converter

## List of figures

Figure 1 Architecture of localization unit of train [7].....	7
Figure 2 Process of fault detection.....	10
Figure 3 - Block scheme for the employed loose integration .....	11
Figure 4 Skyplot of GPS constellation.....	13
Figure 5 Skyplot of dual-constellation of GPS and Galileo.....	13
Figure 6 Results of $P_{md}$ according to the time of detection since position failure.....	14
Figure 7 Expected time of detection according to the heading of train.....	14
Figure 8 Time of detection since position failure according to heading of train .....	15
Figure 9 – How the tests are performed on the loose integration algorithm.....	15
Figure 10 – Sample artificial trajectory used for the tests.....	16
Figure 11 – Urban scenario, positioning errors without integration algorithm .....	18
Figure 12 - Urban scenario, positioning errors without integration algorithm (in function of the travelled distance).....	18
Figure 13 – Urban scenario, positioning error for GNSS only and loosely coupled integration.....	19
Figure 14 - Urban scenario, positioning error for GNSS only and loosely coupled integration (in function of the travelled distance).....	19
Figure 15 – Urban scenario, positioning error in function of the R matrix.....	20
Figure 16 – Urban scenario, positioning error in function of the Q matrix.....	21
Figure 17 – Urban scenario, positioning error when using a balise.....	22
Figure 18 – Suburban scenario, positioning error.....	23
Figure 19 – Open sky scenario, positioning error.....	23
Figure 20 – Dead reckoning positioning error in function of the train velocity.....	24
Figure 21 –Standard FLL adaptive block response to linear chirp: steady-state error (a), settling time (b) and overshoot (c) evaluation as a function of the loop bandwidth $B_n$ , for constant pole contraction factor and sampling frequency, $k\alpha = 0.95$ and $f_s = 40$ MHz. Curves are parameterized on the filter order $K$ . .....	27
Figure 22 – Lower bound of the frequency estimation error, $eLB$ , as a function of the sampling frequency. Curves are parameterized on the sweep rate.....	27
Figure 23 –Settling time evaluation as a function of the loop bandwidth $B_n$ for the first-order exponential FLL and the first-order standard FLL ANFs, for constant pole contraction factor and sampling frequency, $k\alpha = 0.95$ and $f_s = 40$ MHz. ....	28
Figure 24 –ANF response to slow linear chirp: spectrogram evaluation of the input signal (a) and outputs of the exponential filtering FLL ANF (first-order loop) (a) and standard FLL ANF with loop order $K = 1$ (b) and $K = 2$ (c) . The loop bandwidth has be set to $B_n = 3$ MHz. ....	29
Figure 25 –Standard FLL adaptive block response to triangular chirp: steady-state error (a), settling time (b) and overshoot (c) evaluation as a function of the loop bandwidth $B_n$ , for constant pole contraction factor and sampling frequency, $k\alpha = 0.95$ and $f_s = 40$ MHz. Curves are parameterized on the filter order $K$ . ....	30
Figure 26 – Estimated noise jitter for the standard FLL, for loop bandwidth $B_n = 3,6$ MHz, filter order $K = \{1, 2, 3\}$ and a linear chirp – wide sweep-slow. Constant pole contraction factor and sampling frequency, $k\alpha = 0.95$ and $f_s = 40$ MHz, are considered.....	30
Figure 27 – CAF of the interfered signal before (a) and after (b) the interference mitigation.....	32
Figure 28 – $\alpha_{mean}$ and successful acquisition percentage $\gamma$ evaluated as a function of the pole contraction factor $k\alpha$ and the loop bandwidth $B_n$ for the standard FLL and the exponential FLL ANFs respectively in case of $J/N = -1.8$ dB (a)(b), $J/N = 18.2$ dB (c)(d) and $J/N = 25.2$ dB (e)(f). Constant $C/N_0 = 55$ dB – Hz is considered. ....	34

## List of tables

Table 1 GNSS Error model parameters.....	12
Table 2 – Parameters of the trajectories used during the tests .....	16
Table 3 - Urban scenario, positioning error statistics in function of R.....	20
Table 4 - Urban scenario, positioning error statistics in function of Q.....	21
Table 5 - Urban scenario, positioning error statistics when using a balise .....	22
Table 6 - Suburban scenario, positioning error statistics .....	23
Table 7 – Open sky scenario, positioning error statistics.....	24
Table 8 – Main features of the selected jammers, as reported in [RD.3]. .....	26
Table 9 – Comparison of <i>amean</i> measured for the signal filtered, using the FLL-equivalent ANFs with the best parameter settings, against the unfiltered case for several <i>J/N</i> conditions.....	34

## References

- [1] F. Rispoli, G. Sicilano, and C. Brenna, "GNSS for ERTMS train localization: A step-change technology and new business model," InsideGNSS, March-April, pp. 48–54, 2017.
- [2] A. Neri, S. Sabina, F. Rispoli, and U. Mascia, "GNSS and odometry fusion for high integrity and high availability train control systems," in Proceedings of the 28th International Technical Meeting of The Satellite Division of the Institute of Navigation (ION GNSS+ 2015), Tempa, FL, 2015, pp. 639–648.
- [3] S. Lo et al., "Projected Performance of a Baseline High Integrity GNSS Railway Architecture under Nominal and Faulted Conditions," in Proceedings of the 30th International Technical Meeting of The Satellite Division of the Institute of Navigation (ION GNSS+ 2017), Portland, OR, 2017, pp. 2148–2171.
- [4] M. Malvezzi, B. Allotta, and M. Rinchi, "Odometric estimation for automatic train protection and control systems," Vehicle system dynamics, vol. 49, no. 5, pp. 723–739, 2011.
- [5] M. Lauer and D. Stein, "A train localization algorithm for train protection systems of the future," IEEE Transactions on Intelligent Transportation Systems, vol. 16, no. 2, pp. 970–979, 2015.
- [6] UNISIG, ETCS Application Level 1 - Safety Analysis Part 1 - Functional Fault Tree. 2014.
- [7] NGTC, "WP7 Common Understanding Regarding Operational Database Management for Virtual Balises," 2015.
- [8] A. Filip, "Travelling Virtual Balise For ETCS," International Journal of Transport Development and Integration, vol. 1, no. 3, pp. 578–588, 2017.
- [9] C. D. Salos Andrés, "Integrity monitoring applied to the reception of GNSS signals in urban environments," PhD Thesis, Institut national polytechnique, Toulouse, 2013.
- [10] D.-229E RTCA, "Minimum Operational Performance Standards for Global Positioning System/Satellite-Based Augmentation System Airborne Equipment (SBAS MOPS)," 2016.
- [11] B. Pervan, S. Khanafseh, and J. Patel, "Test statistic auto-and cross-correlation effects on monitor false alert and missed detection probabilities," in Proceedings of the 2017 International Technical Meeting of The Institute of Navigation, Monterey, CA, 2017, pp. 562–590.
- [12] D. Kellner, M. Barjenbruch, K. Dietmayer, J. Klapstein, and J. Dickmann, "Joint radar alignment and odometry calibration," in 18th International Conference on Information Fusion, 2015, pp. 366–374.
- [13] U-H2020 Shift2Rail (S2R) project, Available online: <https://shift2rail.org/> (accessed on 10 July 2018)
- [14] A. Neri, S. Sabina, F. Rispoli, and U. Mascia, "GNSS and odometry fusion for high integrity and high availability train control systems," ION GNSS+ 2015
- [15] [online] DEUTA-WERKE GmbH, "DEUTA Radar Sensors", <https://www.deuta.com/en/radar-sensors.aspx> (visited February 2019)
- [16] D. Borio, C. O'Driscoll and J. Fortuny, "GNSS Jammers: Effects and countermeasures," 2012 6th ESA Workshop on Satellite Navigation Technologies (Navitec 2012) & European Workshop on GNSS Signals and Signal Processing, Noordwijk, 2012, pp. 1-7. doi: 10.1109/NAVITEC.2012.6423048
- [17] D. Borio, "Loop analysis of adaptive notch filters," in IET Signal Processing, vol. 10, no. 6, pp. 659-669, 8 2016. doi: 10.1049/iet-spr.2015.0310
- [18] DAVIS, F., Ed., GNSS Interference Threats & Countermeasures. Norwood, MA, USA: Artech House, 2015.
- [19] Falletti, E., Margaria, D., and Motella, B., "A Complete Educational Library of GNSS Signals and Analysis Functions for Navigation Studies," Coordinates, Vol. V, No. 8, August 2009, pp. 30-34.

- [20] Margaria, D., Falletti, E., Motella, B., Pini, M., and Povero, G., "N-FUELS, a GNSS Educational Tool for Simulation and Analysis of a Variety of Signals in Space," Proceedings of the European Navigation Conference on GNSS, ENC-GNSS 2010, Braunschweig, Germany, October 2010.
- [21] Abdizadeh, M., GNSS Signal Acquisition in The Presence of Narrowband Interference, Ph.D. Dissertation, University of Calgary, September 2013.